APPLICATION OF ACOUSTIC RAY TRACING TO DETERMINE SOUND
PATHWAYS INTO THE HUMAN HEAD

BY

JARED A. MCNEW

B.S., University of Wisconsin – Madison, 2006

THESIS

Submitted in partial fulfillment of the requirements
for the degree of Master of Science in Electrical and Computer Engineering
in the Graduate College of the
University of Illinois at Urbana-Champaign, 2008

Urbana, Illinois

Adviser:

Professor William D. O'Brien, Jr.

To my parents.

ACKNOWLEDGMENTS

TABLE OF CONTENTS

LIST OF TABLES

LIST OF FIGURES

LIST OF SYMBOLS

ρ equilibrium density

c speed of sound

α absorption coefficient

p acoustic pressure

f frequency

$\omega = 2\pi f$ angular frequency

$k = \omega/c$ wavenumber

r radial coordinate in spherical coordinate system

θ azimuthal coordinate in spherical coordinate system

ϕ polar coordinate in spherical coordinate system

P_m Legendre polynomial

j_m spherical Bessel function

n_m spherical Neuman function

$h_m^{(k)}$ spherical Hankel function

Re   real part

CHAPTER 1

INTRODUCTION

1.1 Motivation

1.1.1 Noise induced hearing loss

Noised induced hearing loss is hearing loss as a result of exposure to harmful noise. This harmful noise can be either impulse sounds like explosions or long duration exposure such as that experienced on the deck of an aircraft carrier. As a result of this exposure, the hair cells in the cochlea are damaged and cannot be repaired [1]. The Occupational Safety and Health Administration (OSHA) standard 29 CFR 1926.52(d)(1) specifies the permissible noise exposures as a function of the duration of the exposure. The values from this standard are shown in Table 1.1. OSHA standard 29 CFR 1926.52(e) also specifies that exposure to impulse or impact noise should not exceed 140 dB peak SPL.

Table 1.1: OSHA Standard for Permissible Noise Exposures.

Duration Per Day (hours)	Sound Level (dBA slow response)
8	90
6	92
4	95
3	97
2	100
1 1/2	102
1	105
1/2	110
1/4 or less	115

1.1.2 Current hearing protection devices (HPDs)

The majority of HPDs used today can be broken down into two categories: passive and active. Passive devices such as earplugs and earmuffs reduce the sound level reaching the inner ear by blocking the air conduction pathways. Active noise reduction (ANR) devices use noise canceling circuitry and transducers to add an out-of-phase version of the noise so that when summed the noise is cancelled out [2].

Failures of current HPDs

Multiple factors contribute to reduce the effectiveness of passive HPDs when used in the real world. Air leaks between an earplug and the pinna can reduce the attenuation by 5 to 15 dB. Vibration of the HPD can also reduce the attenuation of the device. This occurs in earplugs due to the flexibility of the ear canal which can cause the earplug to vibrate like a piston. This also occurs with earmuffs due the mass-spring system of the earmuff headband and the earmuff cushions. As a result of vibration, the attenuation limit for earmuffs and earplugs at 125 Hz becomes 25 dB and 40 dB, respectively. A less common reduction in attenuation is due to transmission through the material of the HPD. This reduction is most noticeable when using materials with lower attenuation and for earmuffs at certain frequencies. The final factor contributing to the reduced effectiveness of HPDs is bone conduction. Current HPDs are designed to attenuate sound transmission via the air conduction pathways but not the bone conduction pathways. For certain frequencies, bone conduction may become the dominant pathway, thus reducing the effectiveness of the HPD [3].

ANR devices appear to be a promising technology, but devices available today are unable to achieve the performance of passive devices. Earmuffs with ANR added have been shown to improve real-ear attenuation compared to earmuffs or earplugs used by themselves at low frequencies, but the combination of earplugs and earmuffs has better attenuation than the earmuffs with ANR [2].

Crews on aircraft carrier flight decks can be subjected to noise levels as high as 150 dB. Due to limits in attenuation achievable by current HPDs, it is still possible for noise induced hearing loss to occur even when wearing

earplugs and earmuffs due to bone conduction [3, 4]. The goal of this project is to determine the dominant bone conduction pathways. Once these pathways have been determined it may be possible to design HPDs that reduce the sound propagated through them.

1.2 Methods

1.2.1 Finite element analysis (FEA)

The human head is a complex scatterer composed of multiple layers and has a complex geometry. As a result of this, analytic solutions to sound scattering do not exist and a numerical method must be used. The finite element method (FEM) was chosen for this project. The finite element method can compute the approximate solution to scattering from an arbitrary geometry with multiple layers. The idea behind FEM is to divide the continuous volume into a finite number of discrete volumes, called elements. Each of these elements has properties associated with it such as sound speed and density. Each of these elements will have a series of nodes associated with it, each having a position in space associated with it. FEM then uses the equations governing acoustic wave propagation to compute the pressure at these nodes. The pressure between nodes can also be approximated by interpolating the pressure of the surrounding nodes.

The finite element method has other advantages besides the ability to simulate arbitrary volumes. It can also be used to compute solutions to numerous sources such as plane waves and point sources. Both time-harmonic and transient problems can be solved using the finite element method as well.

The finite element method does have some drawbacks, though. The solution step of the finite element procedure requires solving a system of N equations, where N is the number of nodes. In general, as the number of nodes is increased the accuracy of the solution increases. A tradeoff exists between computational efficiency and accuracy. For transient analysis, error can also be introduced if the time step is chosen too large. In general, as the time step decreases, the accuracy increases but requires more computation.

1.2.2 Ray tracing

One method of visualizing the propagation of acoustic energy is ray tracing. Ray tracing is often used in geometrical acoustics when the size of the scatterer is much larger than a wavelength. If this is the case, the full wave equation does not need to be solved and the simpler Eikonal equation is used instead. In doing so, the problem is solved in terms of the propagation of rays instead of waves. For the case of plane wave incidence, a uniform grid of rays normal to the wavefront at time $t = 0$ is drawn. As the wave propagates, these rays are bent according to the Eikonal equation and thus the wave is propagated. If the intensity at time $t = 0$ is I_0 and the density of rays passing through an area at this time is N_0 rays/m^2, and if the density of rays at a time $t = \tau$ is N_1, then the intensity is $N_1 I_0 / N_0$. Thus the areas with high concentrations of rays intersecting the wavefront have a higher intensity [5]. By finding the points with the highest ray density, we can determine the dominant pathways through which sound travels to reach the cochlea.

For the case of the human head, the wavelength is on the order of the size of the human head for audible frequencies. As a result, the small wavelength assumption required for use of the Eikonal equation does not apply to the current problem and the full wave equation must be solved. Even though the Eikonal equation cannot be used, ray tracing can still be performed in the following way. Start with a uniform grid of rays normal to the wavefront at time $t = 0$. Find the intersection of these rays with the wavefront at some small time increment, dt. Next compute the normal to the wavefront at time $t = dt$ at the intersection points. Compute the intersection of these normals with the wavefront at time $t = 2dt$. These two steps are repeated until the end of the domain is reached. The result will be a set of ray paths that can be interpreted in the same way as those computed using the Eikonal equation.

CHAPTER 2

THEORY

2.1 Sound Scattering from Two Concentric Fluid Spheres

In order to verify the ray tracing code, the solution to scattering of plane waves by two concentric fluid spheres is solved. For computational simplicity, the spheres are located at the origin of a spherical coordinate system (r, θ, ϕ) as shown in Fig. 2.1. The source is either a plane wave propagating in the $-z$ direction or a point source located at $(0, 0, R)$. Both source placements eliminate any dependence on ϕ.
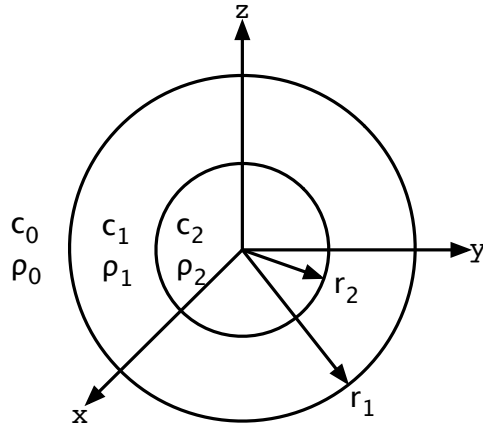
Figure 2.1: Concentric fluid sphere geometry. Infinite medium with density ρ_0, sound speed c_0, and absorption coefficient α_0. The outer sphere has density ρ_1, sound speed c_1, absorption coefficient α_1, and radius r_1. The inner sphere has density ρ_2, sound speed c_2, absorption coefficient α_2, and radius r_2. The spheres are centered at the origin of a spherical coordinate system (r, θ, ϕ) where r is the radial coordinate, θ the azimuthal coordinate, and ϕ the polar coordinate.

The pressure in the medium, p_0, is the sum of the incident pressure p_{0i}, and the scattered pressure p_{0r} [6].

$$p_0 = p_{0i} + p_{0r} \tag{2.1}$$

$$p_{0i} = \mathscr{P}_0 \sum_{m=0}^{\infty} (2m+1)\, \mathscr{L}_m P_m\left(\mu\right) j_m\left((k_0 + i\alpha_0)r\right) e^{-i\omega t} \tag{2.2}$$

$$p_{0r} = \sum_{m=0}^{\infty} A_m P_m\left(\mu\right) h_m^{(1)}\left((k_0 + i\alpha_0)r\right) e^{-i\omega t} \tag{2.3}$$

where $\mu = \cos\left(\theta\right)$ and $\mathscr{L}_m$ is given by [7]

$$\mathscr{L}_m = \begin{cases} (-i)^m, & \text{plane wave} \\ h_m^{(1)}\left((k_0 + i\alpha_0)R\right), & \text{monopole} \end{cases} \tag{2.4}$$

The pressure in the outer sphere, p_1, is the sum of an outward traveling wave p_{1r} and an inward traveling wave p_{1i}.

$$p_1 = p_{1i} + p_{1r} \tag{2.5}$$

$$p_{1i} = \sum_{m=0}^{\infty} B_m P_m\left(\mu\right) h_m^{(2)}\left((k_1 + i\alpha_1)r\right) e^{-i\omega t} \tag{2.6}$$

$$p_{1r} = \sum_{m=0}^{\infty} C_m P_m\left(\mu\right) h_m^{(1)}\left((k_1 + i\alpha_1)r\right) e^{-i\omega t} \tag{2.7}$$

The pressure in the inner sphere can be written as

$$p_{2i} = \sum_{m=0}^{\infty} D_m P_m\left(\mu\right) j_m\left((k_2 + i\alpha_2)r\right) e^{-i\omega t} \tag{2.8}$$

Four boundary conditions are applicable to the current problem. The first involves the pressure at the boundary between the outer sphere and the medium:

$$p_{0i}\left(r_1\right) + p_{0r}\left(r_1\right) = p_{1i}\left(r_1\right) + p_{1r}\left(r_1\right) \tag{2.9}$$

The second boundary condition involves the pressure at the boundary between the inner and outer spheres:

$$p_{1i}\left(r_2\right) + p_{1r}\left(r_2\right) = p_{2i}\left(r_2\right) \tag{2.10}$$

6

The third boundary condition involves the radial velocity at the boundary between the outer sphere and the medium:

$$u_{0,rad}(r_1) = u_{1,rad}(r_1) \tag{2.11}$$

The final boundary condition involves the radial velocity at the boundary between the inner and outer spheres:

$$u_{1,rad}(r_2) = u_{2,rad}(r_2) \tag{2.12}$$

For the time harmonic case, the radial velocity becomes

$$u_{rad} = -\left(\frac{i}{Z_n}\right)p' \tag{2.13}$$

where the $'$ symbol denotes derivative with respect to the total argument and

$$Z_n = \frac{\rho_n c_n}{1 + i\frac{\alpha c_n}{\omega}} \tag{2.14}$$

The radial velocities then become

$$u_{0i} = -\frac{i}{Z_0}\mathscr{P}_0\sum_{m=0}^{\infty}(2m+1)\mathscr{L}_m P_m(\mu)\, j'_m\left(\tilde{k}_0 r\right)e^{-i\omega t} \tag{2.15}$$

$$u_{0r} = -\frac{i}{Z_0}\sum_{m=0}^{\infty}A_m P_m(\mu)\, h_m^{(1)\prime}\left(\tilde{k}_0 r\right)e^{-i\omega t} \tag{2.16}$$

$$u_{1i} = -\frac{i}{Z_1}\sum_{m=0}^{\infty}B_m P_m(\mu)\, h_m^{(2)\prime}\left(\tilde{k}_1 r\right)e^{-i\omega t} \tag{2.17}$$

$$u_{1r} = -\frac{i}{Z_1}\sum_{m=0}^{\infty}C_m P_m(\mu)\, h_m^{(1)\prime}\left(\tilde{k}_1 r\right)e^{-i\omega t} \tag{2.18}$$

$$u_{2i} = -\frac{i}{Z_2}\sum_{m=0}^{\infty}D_m P_m(\mu)\, j'_m\left(\tilde{k}_2 r\right)e^{-i\omega t} \tag{2.19}$$

where $\tilde{k}_n = k_n + i\alpha_n$. The boundary conditions result in the following system

of equations:

$$\frac{\mathscr{P}_0}{Z_0} (2m+1) \mathscr{L}_m j_m' \left(\tilde{k}_0 r_1 \right) + \frac{1}{Z_0} A_m h_m^{(1)\prime} \left(\tilde{k}_0 r_1 \right)$$
$$= \frac{1}{Z_1} B_m h_m^{(2)\prime} \left(\tilde{k}_1 r_1 \right) + \frac{1}{Z_1} C_m h_m^{(1)\prime} \left(\tilde{k}_1 r_1 \right) \quad (2.20)$$

$$\frac{1}{Z_1} B_m h_m^{(2)\prime} \left(\tilde{k}_1 r_2 \right) + \frac{1}{Z_1} C_m h_m^{(1)\prime} \left(\tilde{k}_1 r_2 \right) = \frac{1}{Z_2} D_m j_m' \left(\tilde{k}_2 r_2 \right) \quad (2.21)$$

$$\mathscr{P}_0 (2m+1) \mathscr{L}_m j_m \left(\tilde{k}_0 r_1 \right) + A_m h_m^{(1)} \left(\tilde{k}_0 r_1 \right)$$
$$= B_m h_m^{(2)} \left(\tilde{k}_1 r_1 \right) + C_m h_m^{(1)} \left(\tilde{k}_1 r_1 \right) \quad (2.22)$$

$$B_m h_m^{(2)} \left(\tilde{k}_1 r_2 \right) + C_m h_m^{(1)} \left(\tilde{k}_1 r_2 \right) = D_m j_m \left(\tilde{k}_2 r_2 \right) \quad (2.23)$$

These equations can then be arranged into matrix form:

$$\begin{pmatrix} \frac{h_m^{(1)\prime}\left(\tilde{k}_0 r_1\right)}{Z_0} & \frac{h_m^{(2)\prime}\left(\tilde{k}_1 r_1\right)}{-Z_1} & \frac{h_m^{(1)\prime}\left(\tilde{k}_1 r_1\right)}{-Z_1} & 0 \\ -h_m^{(1)}\left(\tilde{k}_0 r_1\right) & h_m^{(2)}\left(\tilde{k}_1 r_1\right) & h_m^{(1)}\left(\tilde{k}_1 r_1\right) & 0 \\ 0 & \frac{h_m^{(2)\prime}\left(\tilde{k}_1 r_2\right)}{Z_1} & \frac{h_m^{(1)\prime}\left(\tilde{k}_1 r_2\right)}{Z_1} & \frac{j_m'\left(\tilde{k}_2 r_2\right)}{-Z_2} \\ 0 & h_m^{(2)}\left(\tilde{k}_1 r_2\right) & h_m^{(1)}\left(\tilde{k}_1 r_2\right) & -j_m\left(\tilde{k}_2 r_2\right) \end{pmatrix}$$
$$\times \begin{pmatrix} A_m \\ B_m \\ C_m \\ D_m \end{pmatrix} = \begin{pmatrix} \frac{-\mathscr{P}_0}{Z_0} (2m+1) \mathscr{L}_m j_m' \left(\tilde{k}_0 r_1 \right) \\ \mathscr{P}_0 (2m+1) \mathscr{L}_m j_m \left(\tilde{k}_0 r_1 \right) \\ 0 \\ 0 \end{pmatrix} \quad (2.24)$$

The coefficients can then be solved for analytically using Cramer's rule or numerically using LU decomposition.

2.1.1 Verification

By setting the outer sphere to have the same properties of the medium, or setting the two spheres to have the same properties, the problem becomes that of a single sphere of radius a which has the following solution for the plane wave case [8].

The pressure for $r > a$ is

$$p(r, \theta) = \sum_{m=0}^{\infty} \hat{A}_m P_m (\mu) h_m^{(1)} (k_{med} r) e^{-i\omega t}$$

$$+ \mathscr{P}_0 \sum_{m=0}^{\infty} (2m + 1) (-i)^m P_m (\mu) j_m (k_{med} r) e^{-i\omega t} \quad (2.25)$$

and for $r < a$ is

$$p(r, \theta) = \sum_{m=0}^{\infty} \hat{B}_m P_m (\mu) j_m (k_{in} r) e^{-i\omega t} \quad (2.26)$$

This system of equations can be arranged to be of the form

$$\begin{pmatrix} h_m^{(1)} (k_{med} a) & -j_m (k_{sph} a) \\ \frac{1}{\rho_{med} c_{med}} h_m^{(1)\prime} (k_{med} a) & \frac{-1}{\rho_{sph} c_{sph}} j_m' (k_{sph} a) \end{pmatrix} \begin{pmatrix} \hat{A}_m \\ \hat{B}_m \end{pmatrix}$$

$$= \begin{pmatrix} -\mathscr{P}_0 (2m + 1) (-i)^m j_m (k_{med} a) \\ \frac{-1}{\rho_{med} c_{med}} \mathscr{P}_0 (2m + 1) (-i)^m j_m' (k_{med} a) \end{pmatrix} \quad (2.27)$$

where k_{med}, c_{med}, ρ_{med} are properties of the surrounding medium and k_{sph}, c_{sph}, and ρ_{sph} are properties of the fluid sphere with radius a. The solution is then

$$\hat{A}_m = \mathscr{P}_0 (2m + 1)(-i)^m$$
$$\times \frac{(j_m' (k_{med} a) j_m (k_{sph} a) \rho_{sph} c_{sph} - j_m' (k_{sph} a) n_m (k_{med} a) \rho_{med} c_{med})}{-h_m^{(1)\prime} (k_{med} a) j_m (k_{sph} a) \rho_{sph} c_{sph} + j_m' (k_{sph} a) h_m^{(1)} (k_{med} a) \rho_{med} c_{med}} \quad (2.28)$$

$$\hat{B}_m = \mathscr{P}_0 (2m + 1)(-i)^m$$
$$\times \frac{(n_m' (k_{med} a) j_m (k_{med} a) - j_m' (k_{med} a) n_m (k_{med} a)) \rho_{sph} c_{sph}}{-i h_m^{(1)\prime} (k_{med} a) j_m (k_{sph} a) \rho_{sph} c_{sph} + i j_m' (k_{sph} a) h_m^{(1)} (k_{med} a) \rho_{med} c_{med}}$$
$$(2.29)$$

Outer sphere matched to medium

Let the outer sphere be matched to the medium. Then $k_0 = k_1 = k_{med}$, $c_0 = c_1 = c_{med}$, $\rho_0 = \rho_1 = \rho_{med}$. Also, let $r_2 = a$, $k_2 = k_{sph}$, $c_2 = c_{sph}$,

9

$\rho_2 = \rho_{sph}$, and $\mathcal{L}_m = (-i)^m$ so the the problem now becomes equivalent to a plane wave incident on a single fluid sphere of radius a. For the solution to agree with that in [8], the following equations must be satisfied:

For $r > r_1$,

$$\mathcal{P}_0 (2m+1)(-i)^m j_m (k_{med}r) + A_m h_m^{(1)} (k_{med}r)$$
$$= \hat{A}_m h_m^{(1)}(k_{med}r) + \mathcal{P}_0(2m+1)(-i)^m j_m(k_{med}r) \quad (2.30)$$

so

$$A_m = \hat{A}_m \quad (2.31)$$

For $a < r < r_1$,

$$B_m h_m^{(2)}(k_{med}r) + C_m h_m^{(1)}(k_{med}r) =$$
$$\hat{A}_m h_m^{(1)}(k_{med}r) + \mathcal{P}_0(2m+1)(-i)^m j_m(k_{med}r) \quad (2.32)$$

The following identity is then used:

$$h_m^{(1)}(x) + h_m^{(2)}(x) = 2j_m(x) \quad (2.33)$$

Then
$$B_m = \frac{\mathcal{P}_0(2m+1)(-i)^m}{2} \quad (2.34)$$

and
$$C_m = B_m + \hat{A}_m \quad (2.35)$$

For $r < a$,

$$D_m P_m (\mu) j_m (k_{sph}r) = \hat{B}_m P_m (\mu) j_m (k_{sph}r) \quad (2.36)$$

so

$$D_m = \hat{B}_m \quad (2.37)$$

The solution to Eq. (2.24) for the case when the outer sphere is matched

to the medium is

$$A_m = -\mathscr{P}_0(2m+1)(-i)^m$$
$$\times \frac{\left(j'_m\left(k_{sph}a\right)j_m\left(k_{med}a\right)\rho_{med}c_{med} - j'_m\left(k_{med}a\right)j_m\left(k_{sph}a\right)\rho_{sph}c_{sph}\right)}{j'_m\left(k_{sph}a\right)h_m^{(1)}\left(k_{med}a\right)\rho_{med}c_{med} - h_m^{(1)\prime}\left(k_{med}a\right)j_m\left(k_{sph}a\right)\rho_{sph}c_{sph}}$$

$$B_m = \frac{\mathscr{P}_0(2m+1)(-i)^m}{2}$$

$$C_m = -\mathscr{P}_0(2m+1)(-i)^m$$
$$\times \frac{\left(j'_m\left(k_{sph}a\right)h_m^{(2)}\left(k_{med}a\right)\rho_{med}c_{med} - h_m^{(2)\prime}\left(k_{med}a\right)j_m\left(k_{sph}a\right)\rho_{sph}c_{sph}\right)}{2j'_m\left(k_{sph}a\right)h_m^{(1)}\left(k_{med}a\right)\rho_{med}c_{med} - 2h_m^{(2)\prime}\left(k_{med}a\right)j_m\left(k_{sph}a\right)\rho_{sph}c_{sph}}$$

$$D_m = \mathscr{P}_0(2m+1)(-i)^m$$
$$\times \frac{\left(n'_m\left(k_{med}a\right)j_m\left(k_{med}a\right) - j'_m\left(k_{med}a\right)n_m\left(k_{med}a\right)\right)\rho_{sph}c_{sph}}{ij'_m\left(k_{sph}a\right)h_m^{(1)}\left(k_{med}a\right)\rho_{med}c_{med} - ih_m^{(1)\prime}\left(k_{med}a\right)j_m\left(k_{sph}a\right)\rho_{sph}c_{sph}}$$

which satisfy Eqs. (2.30)-(2.37).

Inner and outer spheres matched

Now let the two spheres be matched to each other such that $k_1 = k_2 = k_{sph}$, $c_1 = c_2 = c_{sph}$, and $\rho_1 = \rho_2 = \rho_{sph}$. Also let $k_0 = k_{med}$, $c_0 = c_{med}$, $\rho_0 = \rho_{sph}$, and $\mathscr{L}_m = (-i)^m$. By setting r_1 to a, the problem again becomes the problem of a plane wave incident on a single sphere. The following equations must then be satisfied:

For $r > a$,

$$\mathscr{P}_0\left(2m+1\right)\left(-i\right)^m j_m\left(k_{med}r\right) + A_m h_m^{(1)}\left(k_{med}r\right)$$
$$= \hat{A}_m h_m^{(1)}(k_{med}r) + \mathscr{P}_0(2m+1)(-i)^m j_m(k_{med}r) \quad (2.38)$$

so

$$A_m = \hat{A}_m \quad (2.39)$$

For $a < r < r_2$,

$$B_m h_m^{(2)}(k_{sph}r) + C_m h_m^{(1)}(k_{sph}r) = \hat{B}_m j_m(k_{sph}r) \tag{2.40}$$

so

$$B_m = C_m = \frac{\hat{B}_m}{2} \tag{2.41}$$

For $r < r_2$,

$$D_m j_m(k_{sph}r) = \hat{B}_m j_m(k_{sph}r) \tag{2.42}$$

so

$$D_m = \hat{B}_m \tag{2.43}$$

Solving Eq. (2.24) for the matched spheres case results in the following coefficients:

$$A_m = -\mathscr{P}_0(2m+1)(-i)^m$$
$$\times \frac{\left(j'_m(k_{sph}a)\,j_m(k_{med}a)\,\rho_{med}c_{med} - j'_m(k_{med}a)\,j_m(k_{sph}a)\,\rho_{sph}c_{sph}\right)}{j'_m(k_{sph}a)\,h_m^{(1)}(k_{med}a)\,\rho_{med}c_{med} - h_m^{(1)\prime}(k_{med}a)\,j_m(k_{sph}a)\,\rho_{sph}c_{sph}}$$

$$B_m = \frac{\mathscr{P}_0(2m+1)(-i)^m}{2i}$$
$$\times \frac{\left(n'_m(k_{med}a)\,j_m(k_{med}a) - j'_m(k_{med}a)\,n_m(k_{med}a)\right)\rho_{sph}c_{sph}}{j'_m(k_{sph}a)\,h_m^{(1)}(k_{med}a)\,\rho_{med}c_{med} - h_m^{(1)\prime}(k_{med}a)\,j_m(k_{sph}a)\,\rho_{sph}c_{sph}}$$

$$C_m = \frac{\mathscr{P}_0(2m+1)(-i)^m}{2i}$$
$$\times \frac{\left(n'_m(k_{med}a)\,j_m(k_{med}a) - j'_m(k_{med}a)\,n_m(k_{med}a)\right)\rho_{sph}c_{sph}}{j'_m(k_{sph}a)\,h_m^{(1)}(k_{med}a)\,\rho_{med}c_{med} - h_m^{(1)\prime}(k_{med}a)\,j_m(k_{sph}a)\,\rho_{sph}c_{sph}}$$

$$D_m = \mathscr{P}_0(2m+1)(-i)^m$$
$$\times \frac{\left(n'_m(k_{med}a)\,j_m(k_{med}a) - j'_m(k_{med}a)\,n_m(k_{med}a)\right)\rho_{sph}c_{sph}}{ij'_m(k_{sph}a)\,h_m^{(1)}(k_{med}a)\,\rho_{med}c_{med} - ih_m^{(1)\prime}(k_{med}a)\,j_m(k_{sph}a)\,\rho_{sph}c_{sph}}$$

which satisfy Eqs. (2.38)-(2.43).

2.2 Synthesizing Finite Duration Solutions from Time-Harmonic Solutions

The solution to sound scattering from two concentric fluid spheres shown above is for a time-harmonic excitation at frequency f. This time-harmonic solution has an infinite duration while the wavefront reconstruction techniques presented later on require a finite duration pulse. One can approximate the solution to finite duration pulse excitation from the time-harmonic solution using Fourier analysis. Let $v(t)$ denote the desired pulse and its Fourier transform $V(f)$, where $V(f)$ is zero for $|f|$ greater than f_{bw}. Analytically, $v(t)$ can be synthesized from its Fourier transform as

$$v(t) \quad = \quad \int_{-\infty}^{\infty} V(f)e^{j2\pi ft}dt \tag{2.44}$$

$$= \quad \int_{-f_{bw}}^{f_{bw}} V(f)e^{j2\pi ft}dt \tag{2.45}$$

Computationally this would require an infinite number of frequencies to be added and is therefore not realizable. One solution to this problem is to create a T-periodic version of $v(t)$, $v((t))_T$, where

$$v((t))_T = \sum_{k=-\infty}^{\infty} v(t - kT) \tag{2.46}$$

This periodic version of $v(t)$ therefore has a Fourier series representation,

$$v((t))_T = \sum_{k=-\infty}^{\infty} V[k]e^{j2\pi kt/T} \tag{2.47}$$

where

$$V[k] = \frac{1}{T} \int_{<T>} v((t))_T e^{-j2\pi kt/T} \tag{2.48}$$

Since $v(t)$ is band-limited, $v((t))_T$ is also, so $V[k]$ is zero for $|k| > Tf_{bw}$. As a result, the sum in Eq. (2.47) is now over a finite number of frequencies

$$v((t))_T = \sum_{k=-\lfloor Tf_{bw} \rfloor}^{\lfloor Tf_{bw} \rfloor} V[k]e^{j2\pi kt/T} \tag{2.49}$$

13

Now let $P(r, \theta, \phi, f)$ denote the complex time-harmonic solution for a frequency f to scattering from two concentric spheres derived earlier. One can then find the approximate solution for pulse excitation using the equation

$$p((r, \theta, \phi, t))_T = \sum_{k=-\lfloor Tf_{bw} \rfloor}^{\lfloor Tf_{bw} \rfloor} P(r, \theta, \phi, -k/T)V[k]e^{j2\pi kt/T} \qquad (2.50)$$

Assuming the pressure at (r, θ, ϕ) and the desired pulse are both real-valued, Eq. (2.50) simplifies to

$$p((r, \theta, \phi, t))_T = V[0]P^*(r, \theta, \phi, 0)$$
$$+ 2 \sum_{k=1}^{\lfloor Tf_{bw} \rfloor} \text{Re}\left\{ V[k]P^*(r, \theta, \phi, k/T)e^{j2\pi kt/T} \right\} \qquad (2.51)$$

When using this method for simulation, one must be careful when choosing the period T. Choosing T to be small reduces computation time by limiting the number of frequencies that are added in Eq. (2.51). By reducing this period, though, pulses are effectively impinging on the spheres closer together; so if the solution has a long impulse response, a new pulse will arrive before the last pulse's response died out and time-domain aliasing will occur.

CHAPTER 3

WAVEFRONT RECONSTRUCTION METHODS

Pierce [9] defines a wavefront as "any moving surface along which a waveform feature is being simultaneously received." The first step in performing ray tracing is determining these wavefronts from the time-domain pressure waveforms over the computational domain. Once these waveforms have been computed, one can then proceed to compute the normals and intersections to propagate the rays. Wavefront computation is also the step most prone to errors. These errors are usually the result of multiple reflections or attenuation at interfaces. Multiple approaches to wavefront reconstruction are presented here along with a discussion of how well they are able to handle the various pitfalls of wavefront reconstruction methods.

All of the methods presented here make the same assumptions about the data being used. The data are assumed to have originated from some sort of computational simulation over a uniform square spatial grid in three dimensions with N points per dimension separated by a distance $dx = dy = dz$. Each point (x, y, z) on the grid is assumed to have a time-domain pressure waveform associated with it, denoted as $p(x, y, z, t)$. The source of excitation is assumed to be a finite duration tone pulse $p_{ref}(t)$, although most methods can be used for any finite duration pulse with minor modifications. The incident field is assumed to be a plane wave propagating in the $+z$ direction.

3.1 Spatial Correlation

3.1.1 Method

The idea behind the spatial correlation method is to determine the wavefront at a time τ by finding the z coordinate for each (x, y) pair that maximizes the correlation of $p(x, y, z, t)$ and $p_{ref}(t - \tau)$.

15

3.1.2 Issues

Strong scatterers cause this method to fail due to reduction in the pulse's magnitude. Assume that $p(x, y, z, t)$ is equal to a time-delayed and scaled version of p_{ref} and the excitation is a tone burst. Consider a point (x_0, y_0, z_0) that is the actual wavefront at time t and some other point (x_1, y_1, z_1). Let $p(x_1, y_1, z_1, t) = A_0 p(x_0, y_0, z_0, t - nT)$, where T is the reciprocal of the center frequency of the tone burst, n is an integer, and A_0 is a result of the attenuation due to transmission loss. If A_0 is sufficiently small, it is possible that although the shifted reference pulse is not perfectly aligned with $p(x_1, y_1, z_1, t)$, it will still have a larger correlation with $p_{ref}(t)$ than will $p(x_0, y_0, z_0, t)$. As a result, the wavefront will be incorrectly identified as being located at (x_1, y_1, z_1) instead of (x_0, y_0, z_0).

This method solves for the wavefront directly, but the methods to follow will determine the wavefront indirectly. Instead of finding the wavefront at time τ, the time it takes for the pulse to reach (x, y, z) is determined. The wavefront at a time τ is then the set of (x, y, z) with the same pulse arrival time. This indirect method of determining wavefronts generally is less vulnerable to attenuation as will be explained in the next section.

3.2 Temporal Correlation

3.2.1 Method

The temporal correlation method, like the spatial correlation method, assumes that $p(x, y, z, t)$ is a delayed version of $p_{ref}(t)$. The arrival time τ of the pulse at a position (x, y, z) is then computed by finding the value of τ that maximizes the correlation of $p(x, y, z, t)$ with $p_{ref}(t - \tau)$. Since the magnitudes of both signals being compared do not change from one delay to another, the attenuation issue encountered with the spatial correlation method is no longer a problem. This particular method works quite well when applied to weak scatterers since the assumption that the $p(x, y, z, t)$ is approximately a time delayed version $p_{ref}(t)$ holds.

3.2.2 Example

The reference signal p_{ref} is plotted in Fig. 3.1 and the pressure at a location (x, y, z) is shown in Fig. 3.2. The correlation of $p(x, y, z, t)$ with time-shifted versions of $p_{ref}(t)$ and is plotted in Fig. 3.3. The time-shift corresponding to the largest correlation value is -0.6472 ms. Figure 3.4 shows p_{ref} shifted by -0.6472 ms with $p(x, y, z, t)$. The incident waveform and the shifted reference signal line up correctly and therefore the arrival time was computed correctly.
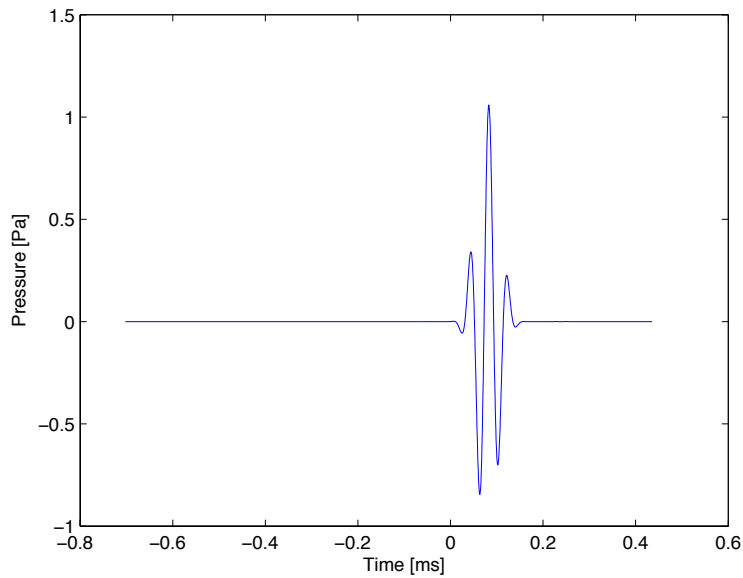

Figure 3.1: Reference signal p_{ref}.

3.2.3 Issues

Reflections and interference can cause significant errors in the results obtained with this method.
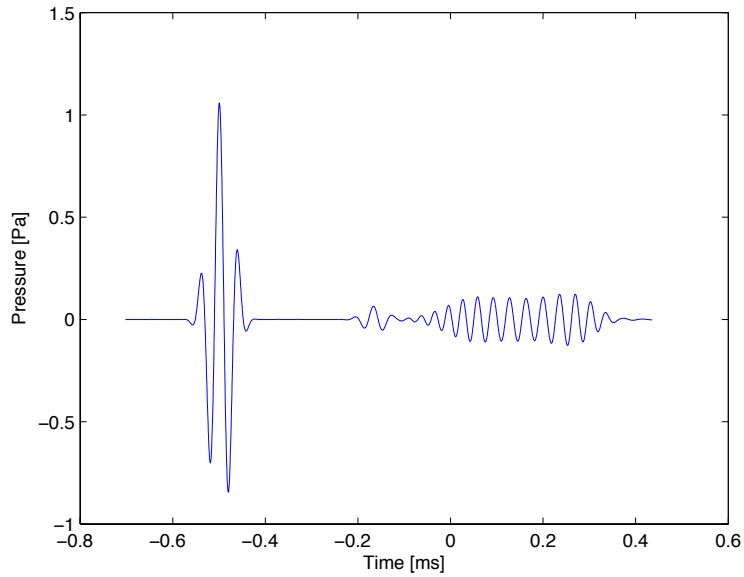
Figure 3.2: Pressure signal for temporal correlation example.
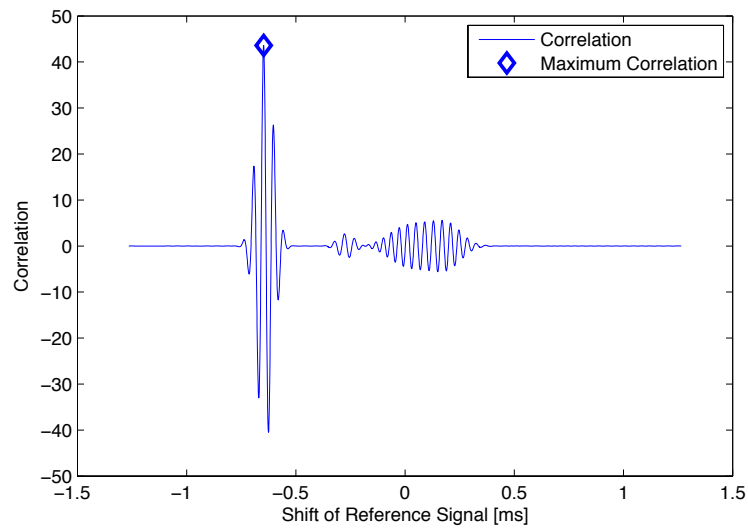
Figure 3.3: Correlation of pressure signal from Fig. 3.2 and time-shifted versions of p_{ref}. The maximum correlation point is marked with a diamond and corresponds to a time shift of -0.6472 ms.
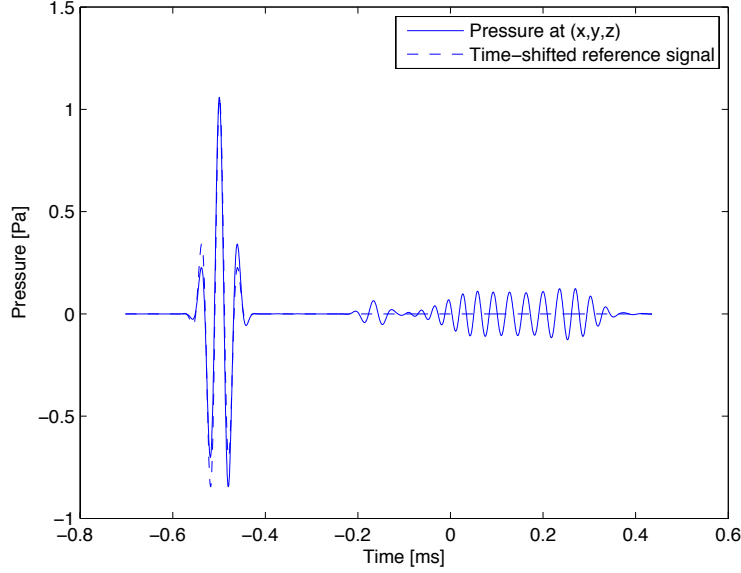
Figure 3.4: Pressure signal from Fig. 3.2 and time-shifted version of reference signal computed using temporal correlation method.

3.3 Minimum Weighted Phase Error

3.3.1 Method

The idea behind the minimum weighted phase error method is observation that the delay of a single frequency component of a signal can be determined by the phase of the Fourier transform of a signal at that frequency. Another observation is that the influence of each frequency component is proportional to the magnitude of the Fourier transform at that frequency. Assume that the $p(x, y, z, t)$ is approximately a time delayed version of $p_{ref}(t)$ after being run through some filter with a phase response of zero. Let $P(x, y, z, f)$ be the Fourier transform of $p(x, y, z, t)$ and $P_{ref}(\tau, f)$ be the Fourier transform of $p_{ref}(t - \tau)$. Define the weighted phase error function $e_\theta(\tau, f)$ as

$$e_\theta(\tau, f) = |\angle P(x, y, z, f) - \angle P_{ref}(\tau, f)| \, |P(x, y, z, f)| \qquad (3.1)$$

The pulse arrival time at the point (x, y, z) is then the value of τ that minimizes the integral of the weighted phase error function over all frequencies.

In equation form,

$$\tau = \underset{t}{\mathrm{argmin}} \left\{ \int_{-\infty}^{\infty} e_\theta(t, f) df \right\} \tag{3.2}$$

3.3.2 Issues

Computation of the unwrapped phase is still an unsolved problem, so the phase computation in Eq. (3.1) is done with the wrapped phase. This can result in a computed phase error that can be either greater or less than the actual value. For example, if $\angle P(x, y, z, f) = 0.99\pi$ the wrapped phase of $p_{ref}(\tau, f)$ is -0.99π, the phase error computed will be 1.98π while the actual phase error is 0.02π since a wrapped phase of -0.99π is equivalent to a phase of 1.01π. On the other hand, if the unwrapped phase of $p(x, y, z, f)$ is 4.1π and the unwrapped phase of $p_{ref}(\tau, f)$ is 2.1π, the unwrapped phase error is 2π while the wrapped phase error is 0. This last point results in significant error in the phase error computation and often results in maxima of $e_\theta(\tau, f)$ occurring at the actual arrival time and also at the arrival time offset by integer multiples of the pitch period for tone burst stimulation.

3.4 Peak Detection

3.4.1 Method

The peak detection uses the first peak of the pulse to be the waveform feature that is tracked over time. The advantage of using the first peak is that this peak is least likely to be distorted by interference patterns. The method works as follows. Set some threshold pressure p_{thr} to be the minimum pressure amplitude that will be considered a peak. This parameter should be chosen so that any noise occurring before the arrival of the pulse is not detected as a peak. Then for a point (x, y, z) find the first t that satisfies $p(x, y, z, t) \geq p_{thr}$. This time will be denoted as t_{thr}. The arrival time τ is then the next local maxima in $p(x, y, z, t)$ such that $\tau \geq t_{thr}$.

3.4.2 Example

Consider the pressure signal at a point (x, y, z) shown in Fig. 3.5. A value of $p_{thr} = 0.15$ is plotted as the dotted line in the figure. The first peak greater than p_{thr} occurs at the point marked by the diamond in the figure. This corresponds to an arrival time of -0.538 ms.
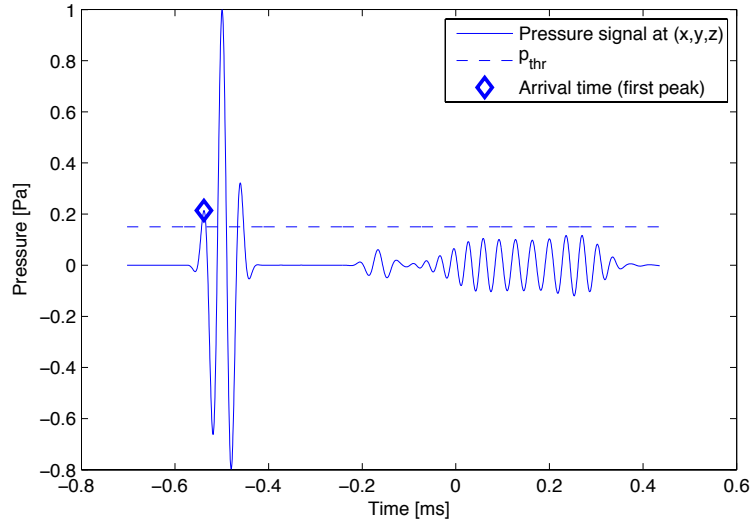

Figure 3.5: Example signal used for the peak detection method. The signal observed at the point (x, y, z) is shown as the solid line, the threshold pressure p_{thr} is the dotted line, and the arrival time is marked by the diamond at -0.538 ms.

3.4.3 Issues

Peaks introduced by noise can result in a false detection of the first peak. If this becomes an issue, a simple solution is to multiply the pressure waveform by its envelope. This will also reduce the magnitude of the first peak, but this reduction will be less than the the reduction of the noise outside of the pulse. It should also be noted that due to attenuation, the $p(x, y, z, t)$ should be normalized to have a maximum of 1 and p_{thr} then becomes the ratio of the noise maximum to the pulse maximum.

3.5 Previous Sample Temporal Correlation

3.5.1 Method

This method is based on the assumption that $p(x, y, z, t)$ is more like a delayed version of $p(x, y, z - dz, t)$ than $p_ref(t)$. This is usually the case, especially when multiple reflections occur. The method is similar to the temporal correlation method except that the correlation is now taken between $p(x, y, z, t)$ and $p(x, y, z - dz, t)$. The difference in arrival times between $z - dz$ and dz is then computed by finding the delay τ of $p(x, y, z - dz, t)$ that maximizes the correlation with $p(x, y, z, t)$. Denote this delay as $\tau_{max}(x, y, z)$. This method is recursive since in order to find the arrival time at a position (x, y, z), the delays from all of the previous z values must be summed.

$$\tau(x, y, z) = \sum_{n=\min\{z\}/dz}^{z/dz} \tau_{max}(x, y, ndz) \tag{3.3}$$

3.5.2 Example

The signals at (x, y, z) and $(x, y, z - dz)$ are shown in Fig. 3.6. The correlation of $p(x, y, z, t)$ with time shifted versions of $p(x, y, z - dz, t)$ is shown in Fig. 3.7 with a maximum at a time shift of 9.443 μs. The pressure at (x, y, z) is plotted with the pressure at $(x, y, z - dz)$ shifted by 9.443 μs in Fig. 3.8. As can be seen from the figure, the shifted version $p(x, y, z - dz, t)$ is aligned with $p(x, y, z, t)$.

3.5.3 Issues

The recursive nature of the method has the drawback that an error in one delay computation for a given (x_0, y_0, z_0) coordinate results in an error in the arrival time for all (x_0, y_0, z) for $z \geq z_0$. Reflections also introduce error, although of a smaller magnitude than the error encountered for the previous correlation based methods. This error results from the fact that when the incident pulses are maximally correlated, the reflected pulses will be slightly out of phase due to their differing path lengths. This correlation of the reflected pulses causes the delay estimate to be less than the actual delay.
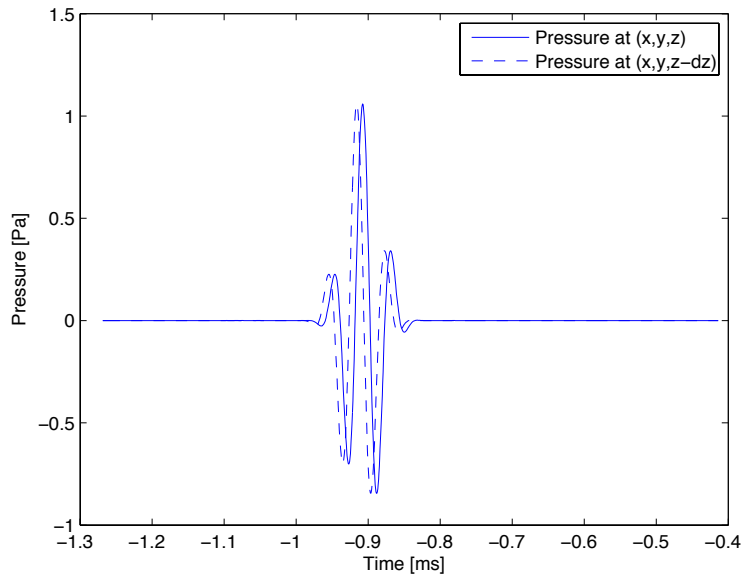
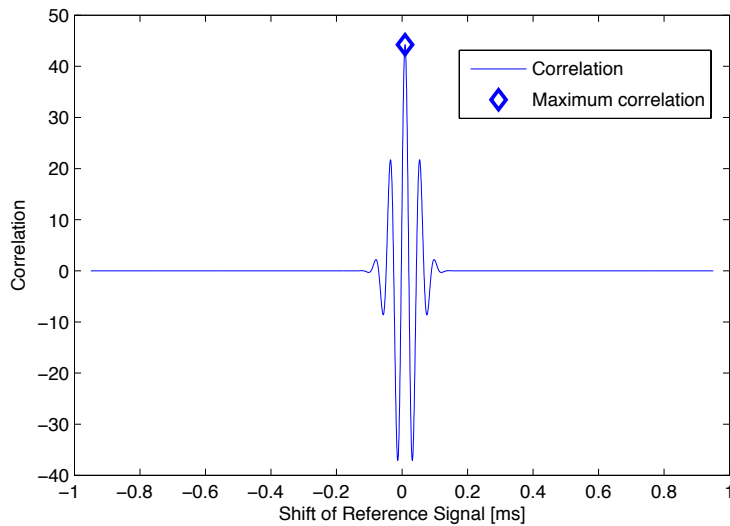Figure 3.6: Pressure signals at (x, y, z) (solid line) and at $(x, y, z-dz)$ (dashed line).

Figure 3.7: Cross-correlation of pressure signal at (x, y, z) with pressure signal at $(x, y, z - dz)$. The diamond indicates the maximum correlation which occurs at a time of 9.443 μs.
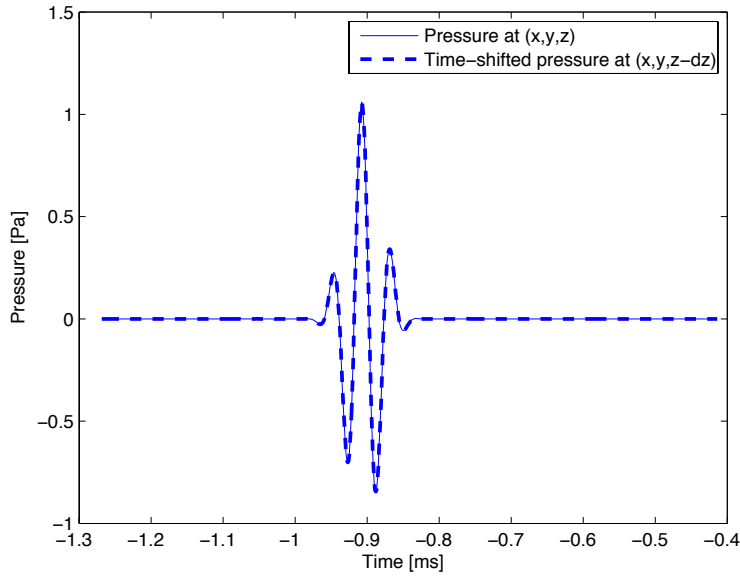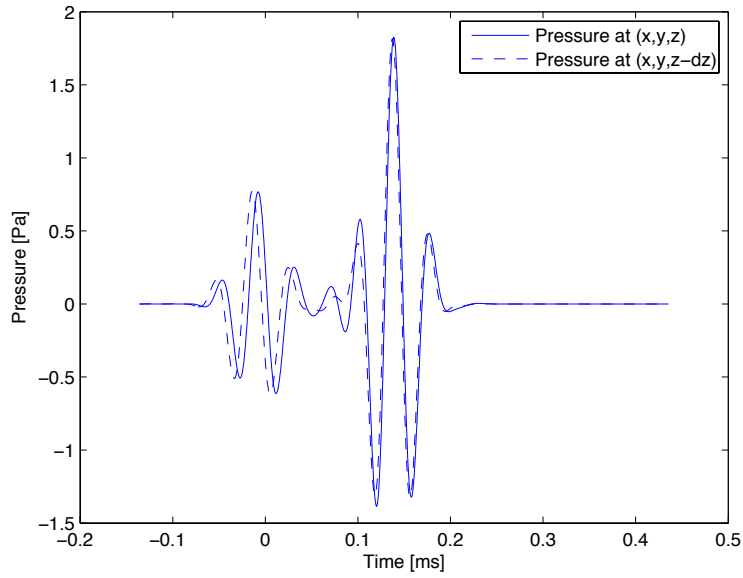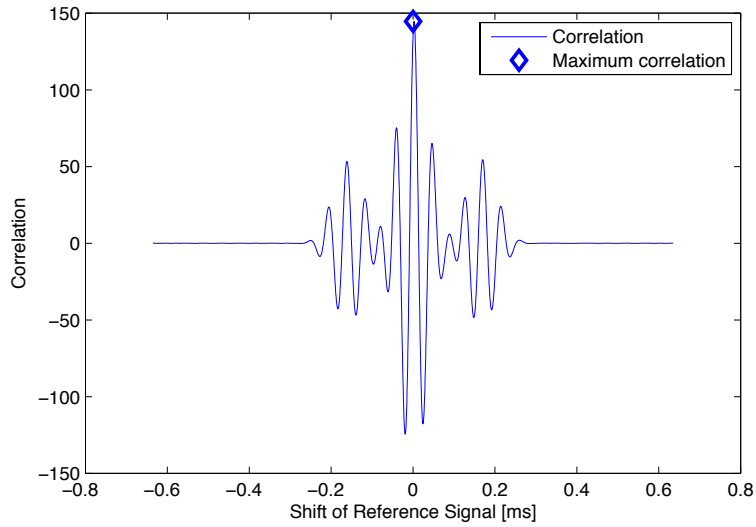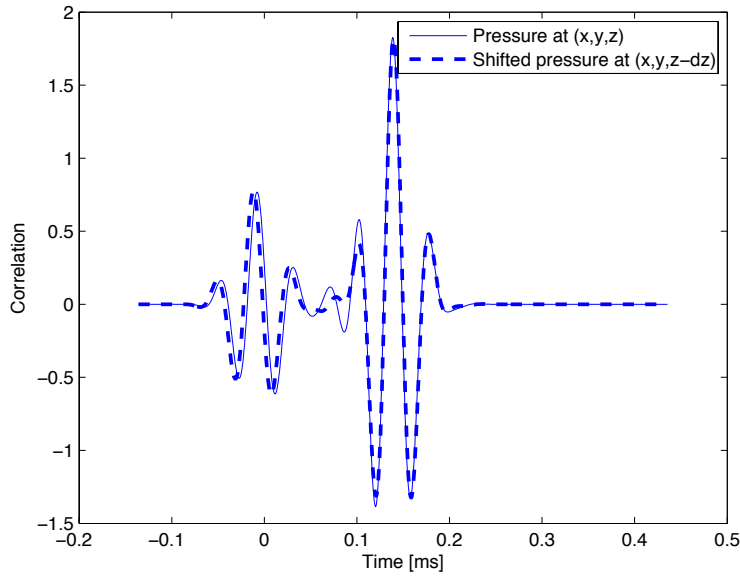
Figure 3.8: $p(x, y, z - dz, t)$ Shifted by the amount found using the last sample temporal correlation method (dashed line) and $p(x, y, z, t)$ (solid line).

The severity of this effect is proportional to the ratio of the magnitude of the reflected pulse to the magnitude of the incident pulse. An example of this is shown in Figs. 3.9-3.11. Figure 3.9 shows $p(x, y, z, t)$ and $p(x, y, z - dz, t)$ when a strong reflected pulse is present. Figure 3.10 shows the cross-correlation of the two signals with a maximum correlation occurring for a shift of 2.518 μs. Figure 3.11 shows $p(x, y, z - dz, t)$ shifted by the value computed with the method and $p(x, y, z, t)$. Looking closely at the figure, it can be seen that the reflected pulse is aligned while the incident pulse is slightly out of phase.

3.6 Previous Sample Temporal Correlation with First Peak Alignment Correction

3.6.1 Method

This method combines the peak detection method with the previous sample temporal correlation method to improve the method's ability to compensate

Figure 3.9: Pressure signals at (x, y, z) (solid line) and at $(x, y, z-dz)$ (dashed line) with reflections.

Figure 3.10: Cross-correlation of pressure signal at (x, y, z) with pressure signal at $(x, y, z - dz)$ with reflections. The diamond indicates the maximum correlation which occurs at a time of 2.518 μs.

Figure 3.11: $p(x, y, z - dz, t)$ Shifted by the amount found using the last sample temporal correlation method (dashed line) and $p(x, y, z, t)$ (solid line) with reflections.

for noise and interference. The first step is to perform the previous sample temporal correlation method to get a rough estimate of the arrival time. The peak detection method is then applied subject to the constraint that the absolute difference in arrival times from $(x, y, z - dz)$ and (x, y, z) must be less than some maximum delay. In this case, the maximum delay is the maximum time it should take to travel a distance of dz multiplied by some tolerance factor greater than 1. If c_{min} is the minimum sound speed over the domain and A_{tol} is the tolerance factor, the maximum delay τ_{max} is then

$$\tau_{max} = \frac{A_{tol} dz}{c_{min}} \tag{3.4}$$

If the delay is not within this tolerate range, the previous sample temporal correlation method is used to approximate the delay between the last sample and the current sample.

3.6.2 Issues

This method results in more accurate arrival determination than either of the methods used on their own. When the first peak method fails and the previous sample temporal correlation must be used, the solution is not exact but is more accurate than would be found using the first peak method. One issue arises as a result of the use of the previous sample temporal correlation method. Since this method has a tendency to underestimate the actual delay, if used on enough samples in a row, the peak detection method may be detected as outside of the allowed delay when the correct arrival time was found.

CHAPTER 4

RAY COMPUTATION

Ray computation is the second stage of the ray tracing procedure and is composed of two steps. First, the normal to the current wavefront is computed. Then the intersection of this normal vector with the next wavefront is found. This process is repeated until the last wavefront is reached. For all examples shown here, the previous sample temporal correlation with first peak alignment correction method is used for wavefront reconstruction.

4.1   Normal Computation

The x and y values of the computational domain are assumed to be on a uniform spatial grid of $N \times N$ points separated by a distance $dx = dy$. The wavefront at a time t and position (x, y) will be denoted as $z(x, y, t)$. To compute the normal to the wavefront at a time t and x and y coordinates (x_0, y_0), first find the x and y coordinates on the computational grid that are closest to x_0 and y_0, respectively. This coordinate will be referred to as (x_q, y_q) and has corresponding wavefront value $z(x_q, y_q, t)$. The points surrounding (x_q, y_q) are then used to form four triangles, as shown in Fig. 4.1, where

$$P_{m,n} = (x_q, y_q, z(x_q, y_q, t)) \tag{4.1}$$

$$P_{m-1,n} = (x_q - dx, y_q, z(x_q - dx, y_q, t)) \tag{4.2}$$

$$P_{m,n-1} = (x_q, y_q - dy, z(x_q, y_q - dy, t)) \tag{4.3}$$

$$P_{m+1,n} = (x_q + dx, y_q, z(x_q + dx, y_q, t)) \tag{4.4}$$

$$P_{m,n+1} = (x_q, y_q + dy, z(x_q, y_q + dy, t)) \tag{4.5}$$

The normal is then computed by taking the cross product of two vectors
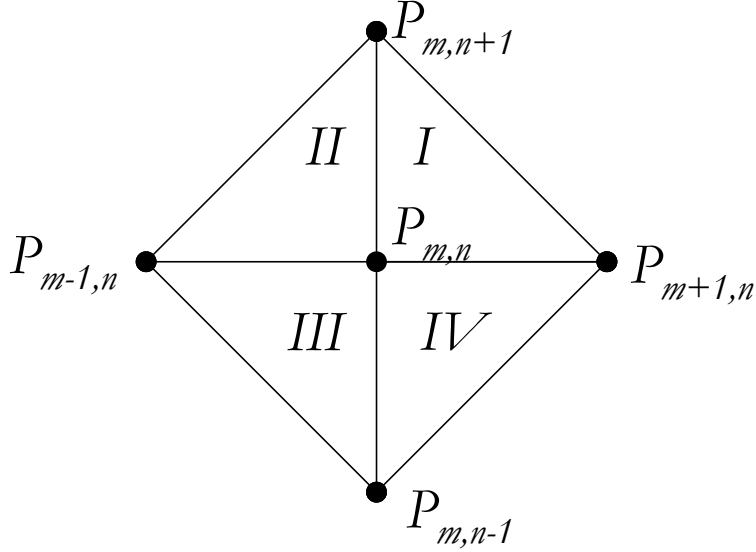
Figure 4.1: Triangles used to determine normal vector.

formed from the sides of the triangle containing $(x, y, z(x, y, t))$. For example if $(x, y, z(x, y, t))$ is located in triangle I, define $\mathbf{v_1} = P_{m+1,n} - P_{m,n}$ and $\mathbf{v_2} = P_{m,n-1} - P_{m,n}$. The normal vector $\mathbf{n}$ is then $\mathbf{v_1} \times \mathbf{v_2}$.

4.2 Intersection Computation

The intersection of the normal with the next wavefront is approximated by finding the intersection of the normal with a triangle formed by the discretized wavefront. Similar to what was done for the normal computation, the triangle closest to the intersection point must first be found. Let $(x_l, y_l, z(x_l, y_l, t))$ correspond to the wavefront at time t over the discretized domain. For all points over the domain find the vector $\mathbf{v_l}$ from the last intersection $(x_0, y_0, z(x_0, y_0, t))$ to each point on the next wavefront. The point which minimizes the magnitude of the error vector $\mathbf{e}$,

$$\mathbf{e} = \frac{\mathbf{n}}{|\mathbf{n}|} - \frac{\mathbf{v_l}}{|\mathbf{v_l}|} \tag{4.6}$$

is the point on the grid closest to the intersection and will be called $P_{m,n}$. The triangle containing the intersection is then found based on the direction of $\mathbf{e}$, similar to what was done for the normal computation. For example, if the

29

x component of **e** is positive and the y component of **e** is negative, triangle IV of Fig. 4.1 is used. The intersection of normal with the wavefront is then approximated as the intersection of the normal with this triangle. Let $a = (x_a, y_a, z_a)$, $b = (x_b, y_b, z_b)$, and $c = (x_c, y_c, z_c)$ be the three vertices of the triangle. The intersection of the normal with the wavefront is then [10]

$$(x_0 + n_x s, y_0 + n_y s, z_0 + n_z s) \tag{4.7}$$

where s can be found by solving the equation

$$\begin{bmatrix} x_0 - x_a \\ y_0 - y_a \\ z_0 - z_a \end{bmatrix} = \begin{bmatrix} -n_x & x_b - x_a & x_c - x_a \\ -n_y & y_b - y_a & y_c - y_a \\ -n_z & z_b - z_a & z_c - z_a \end{bmatrix} \begin{bmatrix} s \\ u \\ v \end{bmatrix} \tag{4.8}$$

4.3 Increasing Normal Accuracy

The discretization of the domain and resulting wavefronts result in normals computed from the wavefronts only being able to take on discrete directions. For example, consider the two dimensional case. The normal shown in Fig. 4.2(a) occurs when the wavefronts at x and $x + dx$ have the same value. The normal shown in Fig. 4.2(b) occurs when the wavefront at x is dz greater than the wavefront at $x + dx$. The normal shown in Fig. 4.2(c) occurs when the wavefront at x is $2dz$ greater than the wavefront at $x + dx$. This pattern can be repeated when the wavefront at x is mdz greater than the wavefront at $x + dx$, where m is an integer. Since propagation is assumed in the $+z$ direction, the normals shown in Figs. 4.2(a) and 4.2(b) occur most frequently. The normal should be able to take on any angle from 0 to 90° with respect to the x-axis but due to quantization it is only able to take on values of $\tan^{-1}(1/m)$. This can lead to significant error in ray tracing computations. A method of reducing this error is presented next.

One method of decreasing the error in the normal computation is to compute the arrival times rounded to an integer multiple of some sampling period T. Let the arrival time at position (x, y, z) be NT and the arrival time at position $(x, y, z + dz)$ be MT, where M and N are integers and $M > N$. One can then use linear interpolation of the wavefronts for the time intervals between. For example, let the arrival time at (x, y, z) be $8T$ and the

(a) $\mathbf{n} = \hat{z}$.   (b) $\mathbf{n} = \hat{x} + \hat{z}$.   (c) $\mathbf{n} = 2\hat{x} + \hat{z}$.
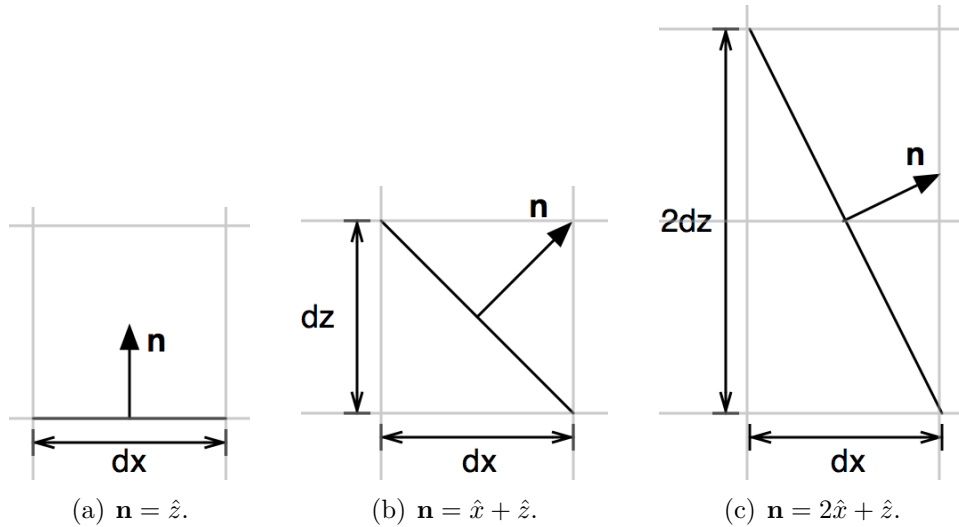
Figure 4.2: Quantized wavefront normals.

arrival time at $(x, y, z + dz)$ be $12T$. The wavefront at time $9T$ can then be approximated as $(x, y, z) + (0, 0, (9-8)dz/(12-8)) = (x, y, z+0.25dz)$. Figure 4.3 shows the new wavefronts found using interpolation for this example. Due to this interpolation step, allowable angles are now $\tan^{-1}((M-N)/m)$ which should increase the accuracy of the ray tracing.
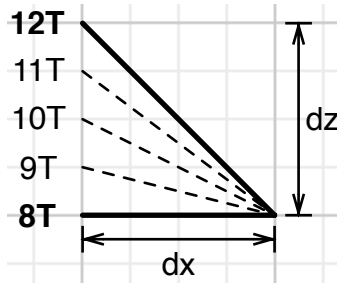
Figure 4.3: Wavefronts found using wavefront interpolation. Wavefronts found without interpolation are shown in bold and additional wavefronts found using interpolation are shown as dashed lines.

4.4   Verification with Snell's Law

In order to validate the ray tracing methods presented above, simulations were performed and then compared to Snell's law. Snell's law states that for

oblique incidence of a plane wave on a planar boundary as shown in Fig. 4.4,
$c_2 \sin(\theta_i) = c_1 \sin(\theta_t)$.
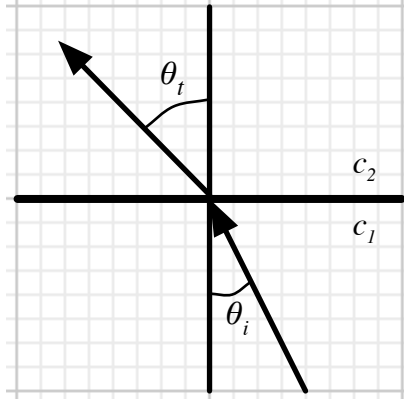
Figure 4.4: Angle and sound speed conventions for Snell's law. θ_i is the angle of incidence, θ_t is the transmission angle, c_1 is the sound speed in the first medium and, c_2 is the sound speed in the second medium.

For the case of the spherical scatterer, the boundary is no longer a plane but can be thought of as a plane tangent to the sphere at the point of intersection of the ray with the sphere as shown in Fig. 4.5. It can be shown that a ray starting at (x, y) and pointing in the $+z$ direction will have an angle of incidence of

$$\theta_i = \sin^{-1}\left(\frac{\sqrt{x^2 + y^2}}{r}\right) \tag{4.9}$$

where r is the radius of the sphere. After applying Snell's law, the angle of transmission will then be

$$\theta_t = \sin^{-1}\left(\frac{c_2}{c_1}\frac{\sqrt{x^2 + y^2}}{r}\right) \tag{4.10}$$

Define the difference angle θ_d as the difference between θ_t and θ_i,

$$\theta_d = \theta_t - \theta_i \tag{4.11}$$

Since the propagation direction is in the positive z direction, θ_d is the angle between the transmitted ray and the positive z-axis. One can then compute the transmitted ray according to Snell's law as follows. First, compute θ_i, θ_t,
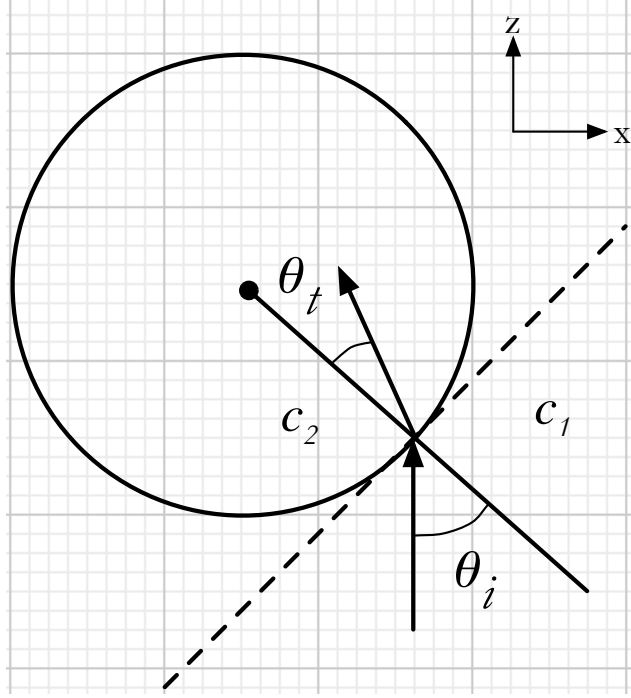
Figure 4.5: Snell's law applied to a plane wave incident on a sphere.

and θ_d as described above. Next, compute the transmitted ray in the $z - x$ plane, which is

$$\mathbf{r_{zx}} = \hat{x}\sin(\theta_d) + \hat{z}\cos(\theta_d) \tag{4.12}$$

The ray must then be rotated about the z-axis by the angle θ_r where

$$\theta_r = \tan^{-1}\left(\frac{y}{x}\right) \tag{4.13}$$

This rotation can be applied using a transformation matrix

$$
\begin{bmatrix} r_x \\ r_y \\ r_z \end{bmatrix} = \begin{bmatrix} \cos(\theta_r) & -\sin(\theta_r) & 0 \\ \sin(\theta_r) & \cos(\theta_r) & 0 \\ 0 & 0 & 1 \end{bmatrix} \begin{bmatrix} \sin(\theta_d) \\ 0 \\ \cos(\theta_d) \end{bmatrix} \tag{4.14}
$$

where the transformed ray is $\hat{x}r_x + \hat{y}r_y + \hat{z}r_z$. The resulting direction of the transmitted ray according to Snell's law is

$$\mathbf{r_{Snell}} = \hat{x}\sin(\theta_d)\cos(\theta_r) + \hat{y}\cos(\theta_d)\sin(\theta_r) + \hat{z}\cos(\theta_d) \tag{4.15}$$

The error of the ray found with the ray tracing code can now be computed.

First, define a vector $\mathbf{v}$, which is the vector starting at the intersection of the computed ray path with the sphere and ending at some point on the computed ray path after the ray has entered the sphere. The error angle θ_e is then computed by finding the angle between $\mathbf{r_{Snell}}$ and $\mathbf{v}$ using the following equation:

$$\theta_e = \cos^{-1}\left(\frac{\mathbf{r_{Snell}} \cdot \mathbf{v}}{|\mathbf{r_{Snell}}||\mathbf{v}|} \right) \tag{4.16}$$

4.4.1 Verification simulation 1

The first simulation used for verification was a 75 mm diameter sphere with a sound speed of 310 m/s and density of 1.21 kg/m^3 surrounded by a medium with a sound speed of 300 m/s and a density of 1.21 kg/m^3. A 12.5 kHz four-cycle sinusoidal pulse was used. Two renderings of the ray paths are shown in Fig. 4.6. The ray tracing error as a function of angle of incidence is plotted in Fig. 4.7.

4.4.2 Verification simulation 2

The second simulation used for verification was a 75 mm diameter sphere with a sound speed of 330 m/s and density of 1.21 kg/m^3 surrounded by a medium with a sound speed of 300 m/s and a density of 1.21 kg/m^3. A 12.5 kHz four-cycle sinusoidal pulse was used. Two renderings of the ray paths are shown in Fig. 4.8. The ray tracing error as a function of angle of incidence is plotted in Fig. 4.9.

4.4.3 Verification simulation 3

The third simulation used for verification was a 75 mm diameter sphere with a sound speed of 400 m/s and density of 1.21 kg/m^3 surrounded by a medium with a sound speed of 300 m/s and a density of 1.21 kg/m^3. A 12.5 kHz four-cycle sinusoidal pulse was used. Two renderings of the ray paths are shown in Fig. 4.10. The ray tracing error as a function of angle of incidence is plotted in Fig. 4.11. As can be seen from the plot, the error is significantly larger than was observed for the 310 m/s sphere. One factor contributing to this error may be the fact that Snell's law only applies when the wavelength
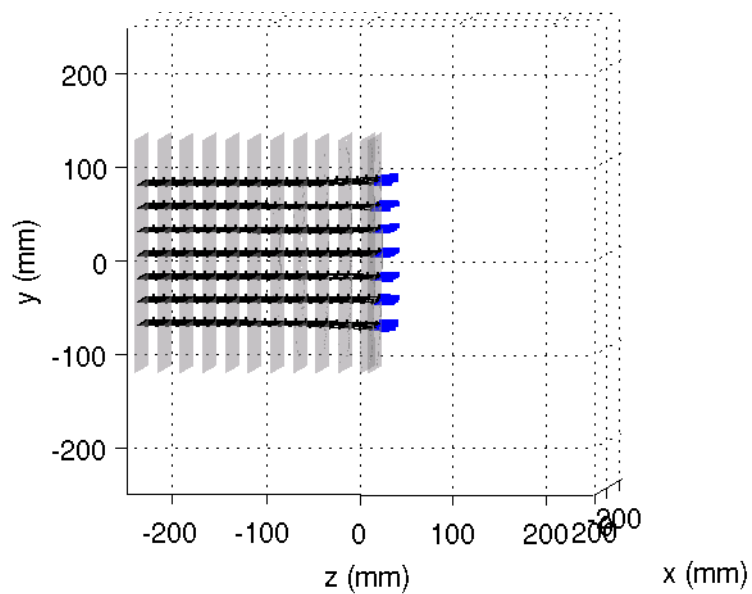
(a) Side View
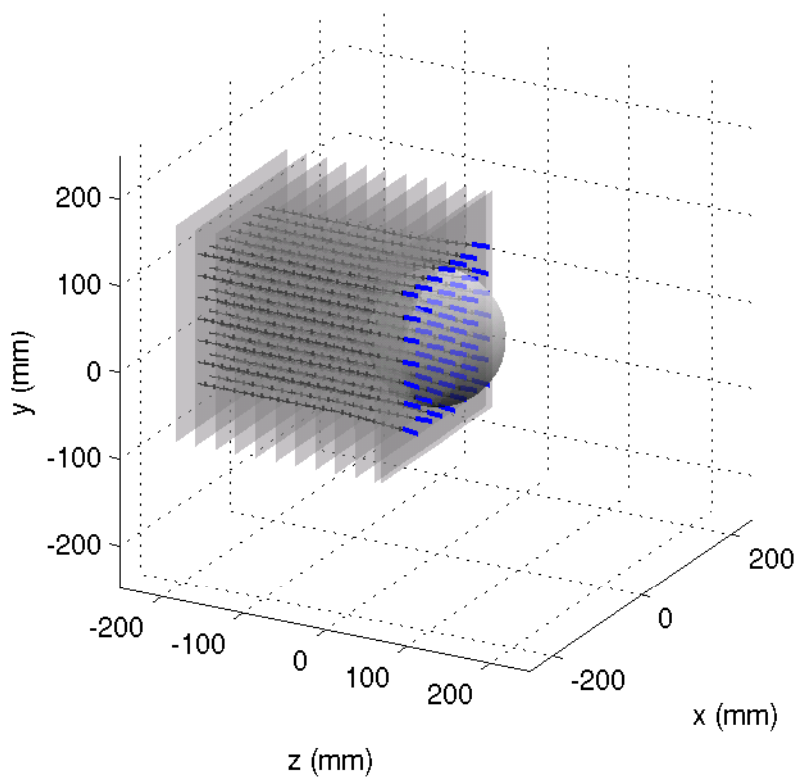
(b) Perspective View

Figure 4.6: Ray tracing for 310 m/s sphere in 300 m/s medium and 12.5 kHz pulse.
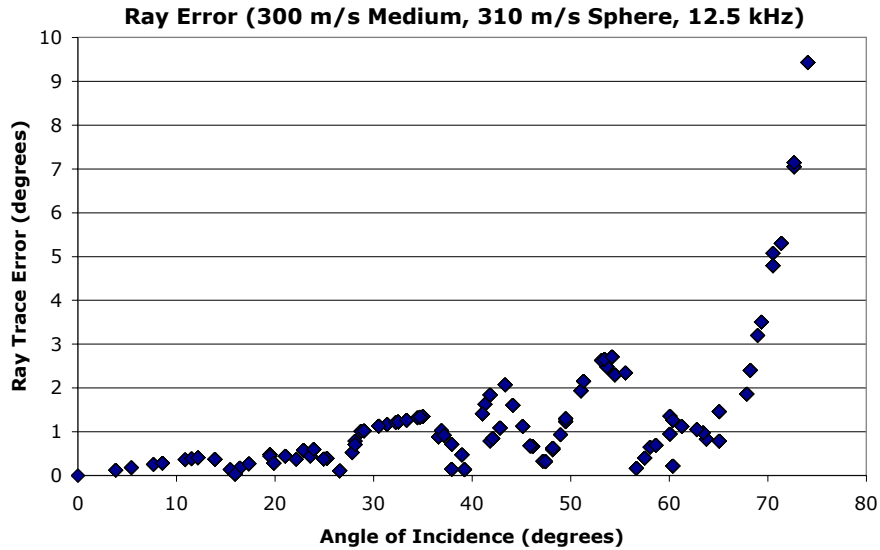
Figure 4.7: Ray tracing error for 310 m/s sphere in 300 m/s medium with matched densities.

approaches zero. In order to verify that this is the source of some of the error, another simulation was performed.

4.4.4 Verification simulation 4

The fourth simulation used for verification was the same as the second except the frequency of the pulse was doubled to halve the wavelength. With this smaller wavelength, the small wavelength assumption of Snell's law should be better satisfied and hence a smaller error observed. Two renderings of the ray paths are shown in Fig. 4.12. The error as a function of the angle of incidence is plotted in Fig. 4.13. Comparison to Fig. 4.11 shows that the error is reduced as the wavelength is made smaller.

4.4.5 Verification simulation 5

The fifth simulation used for verification was a 75 mm diameter sphere with a sound speed of 500 m/s and density of 1.21 kg/m^3 surrounded by a medium with a sound speed of 300 m/s and a density of 1.21 kg/m^3. A 15 kHz four-cycle sinusoidal pulse was used. Two renderings of the ray paths are shown
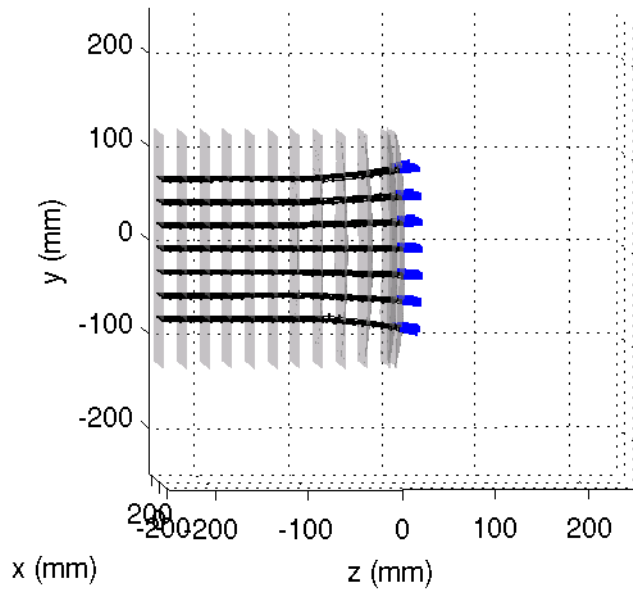
(a) Side View
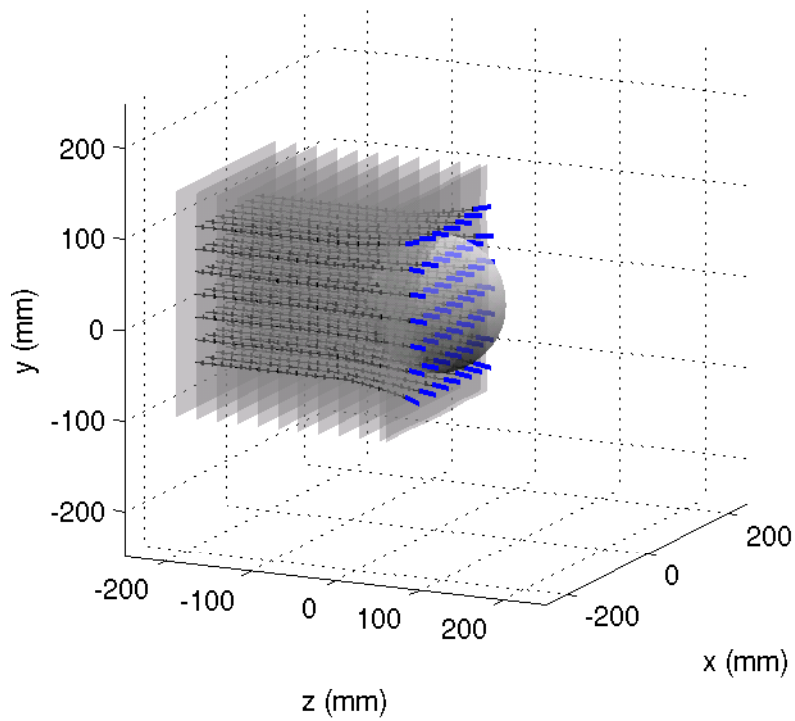
(b) Perspective View

Figure 4.8: Ray tracing for 330 m/s sphere in 300 m/s medium and 12.5 kHz pulse.
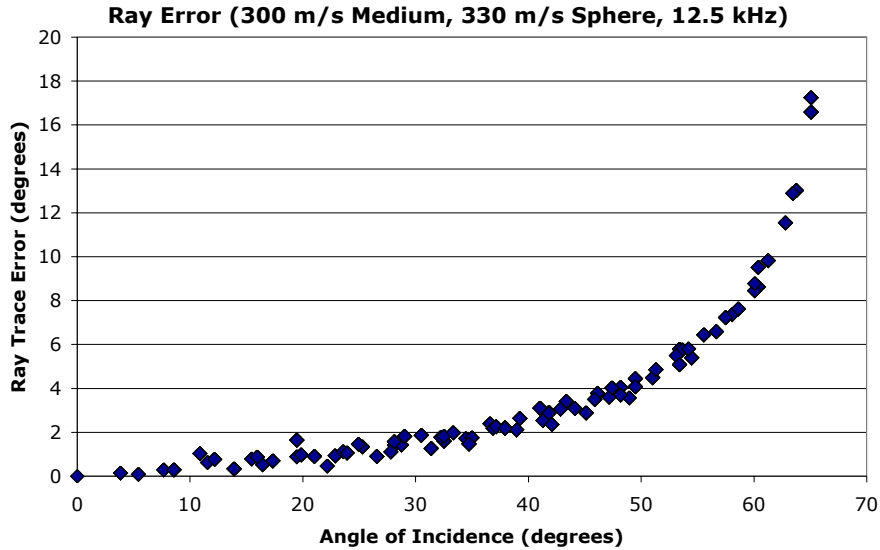
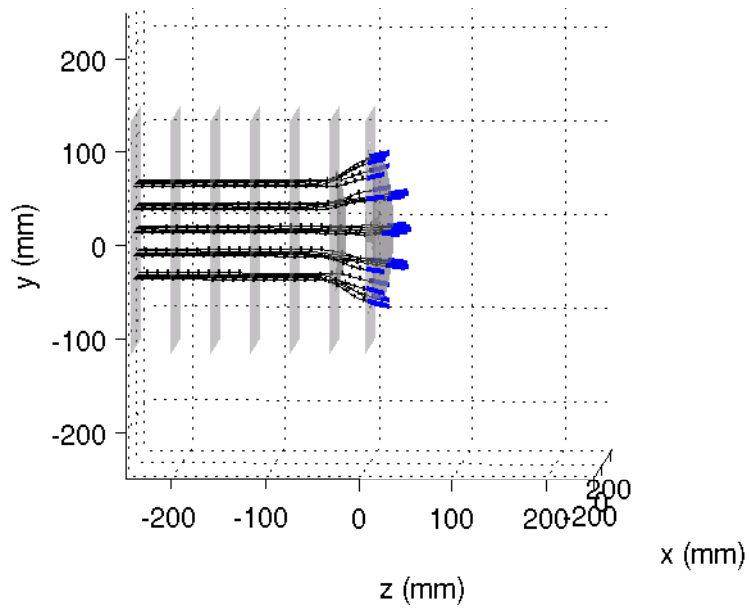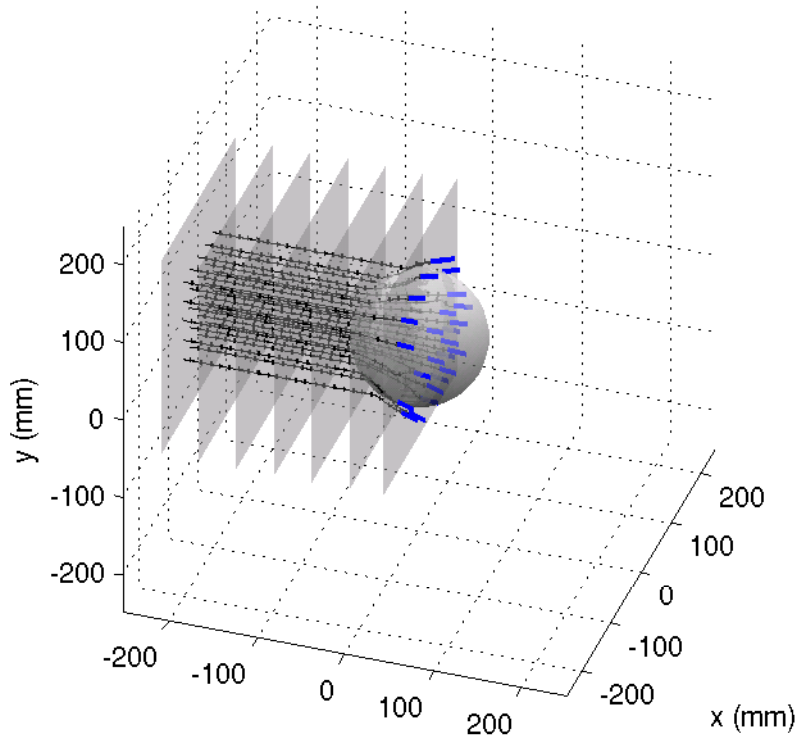Figure 4.9: Ray tracing error for 330 m/s sphere in 300 m/s medium with matched densities.

in Fig. 4.14. The ray tracing error as a function of angle of incidence is plotted in Fig. 4.15.

4.5 Additional Simulations

4.5.1 Concentric fluid spheres

A simulation was performed using the concentric sphere solution with the properties close to that of the human head. A summary of the values used is shown in Table 4.1. The center frequency of the pulse was 1 kHz. Renderings of the ray tracing at six time steps are shown in Fig. 4.16. Higher resolution versions of these images can be found in the Appendix, Figs. A.1 to A.6. Figure 4.17 shows the rays looking into the $-z$ axis to display the ray concentrations better.

The initial concentration of rays is 16 rays per 400 mm^2 which is shown in Fig. 4.17(a). The second time step is shown in Fig. 4.17(b). Near the bone-air interface the concentration of rays doubles to 32 rays per 400 mm^2, corresponding to having twice the initial intensity in that region. Inside the

38
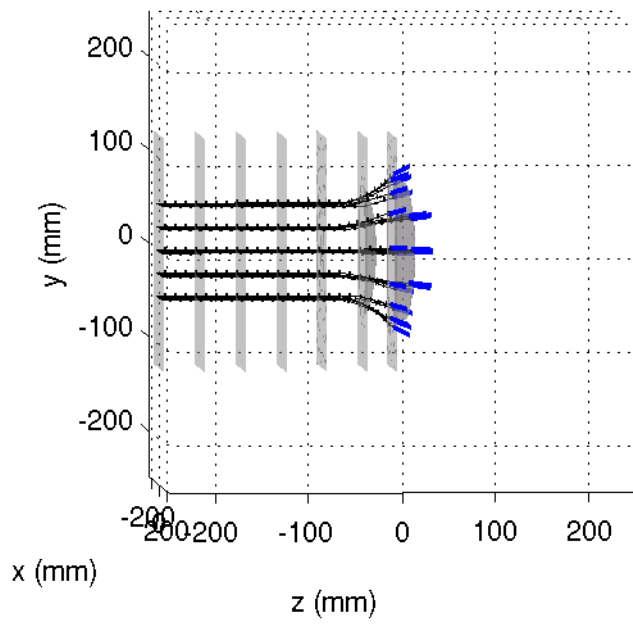
(a) Side View
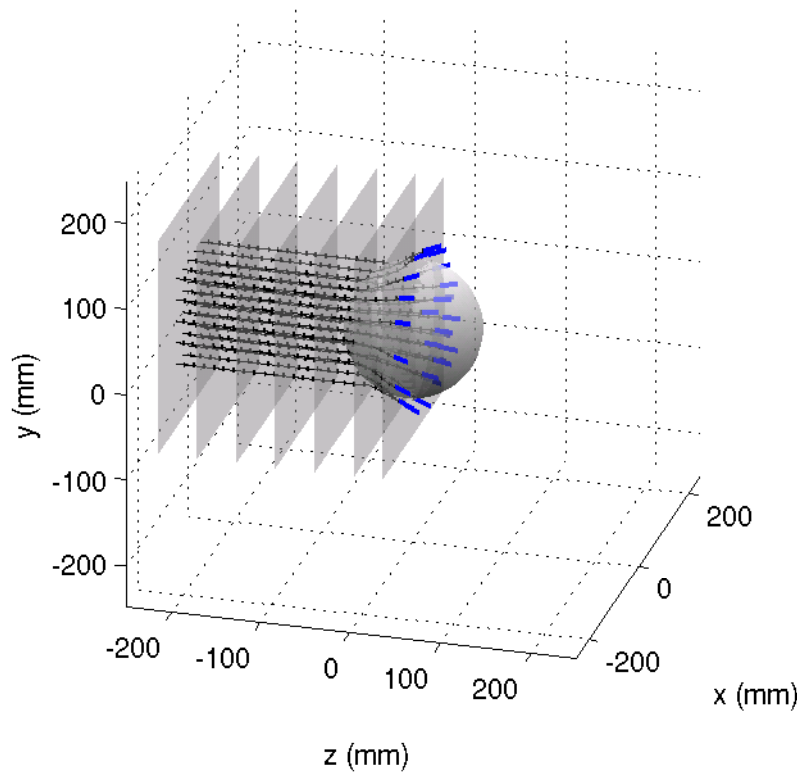
(b) Perspective View

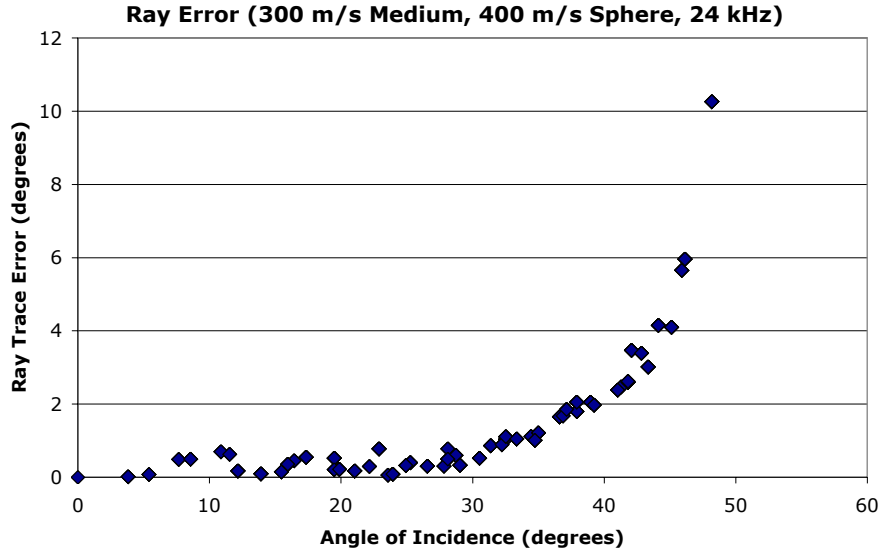Figure 4.10: Ray tracing for 400 m/s sphere in 300 m/s medium and 12.5 kHz pulse.
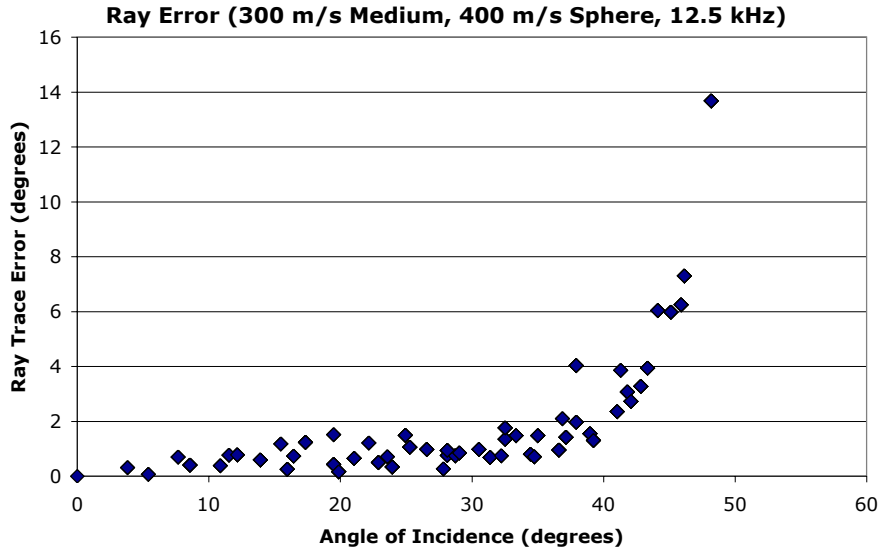
Figure 4.11: Ray tracing error for 400 m/s sphere in 300 m/s medium with matched densities for a 12.5 kHz pulse.

brain region the concentration of rays is reduced by roughly a factor of four to 3 rays per 400 mm^2, corresponding to an intensity that is a quarter of the initial intensity. The third time step is shown in Fig. 4.17(c). Near the bone-air interface the concentration of rays is 31 rays per 400 mm^2 which is still roughly twice the initial concentration. Inside the brain region the concentration of rays is as low as 0.5 rays per 400 mm^2, which has a corresponding intensity of approximately 3% of the initial intensity. The fourth time step is shown in Fig. 4.17(d). Near the bone-air interface the concentration of rays is 28 ray per 400 mm^2, which corresponds to an intensity of 1.75 times the initial intensity. Inside the brain region the concentration of rays is still as low as 0.5 rays per 400 mm^2, which has the corresponding intensity of 3% of the initial intensity. The fifth time step is shown in Fig. 4.17(e). Near the bone-air interface the concentration of rays is 26 rays per 400 mm^2, which corresponds to an intensity of 1.625 times the initial intensity. Inside the brain region the concentration of rays is as low as 1 ray per 400 mm^2, which corresponds to an intensity of approximately 6% of the initial intensity. The sixth time step is shown in Fig. 4.17(f). Near the bone-air interface the concentration of rays is 28 rays per 400 mm^2, which corresponds to an intensity of 1.75 times the initial intensity.

40

(a) Side View

(b) Perspective View

Figure 4.12: Ray tracing for 400 m/s sphere in 300 m/s medium and 24 kHz pulse.

41

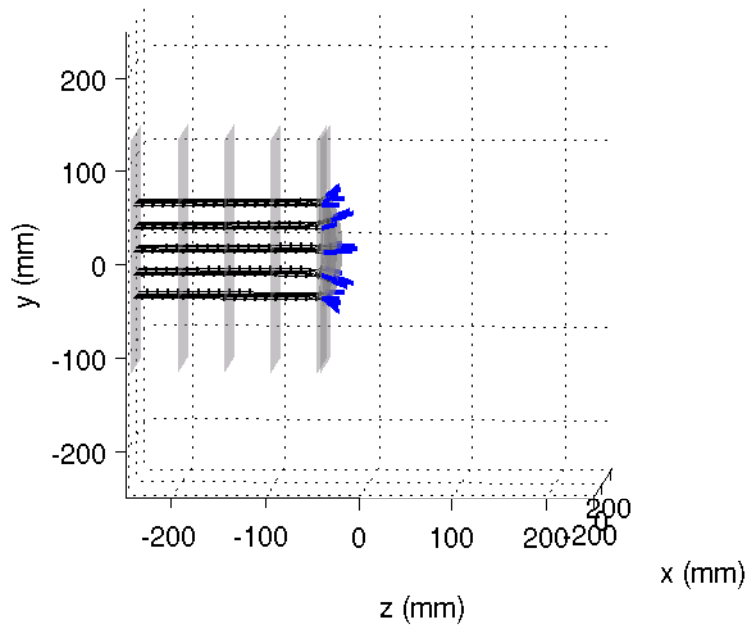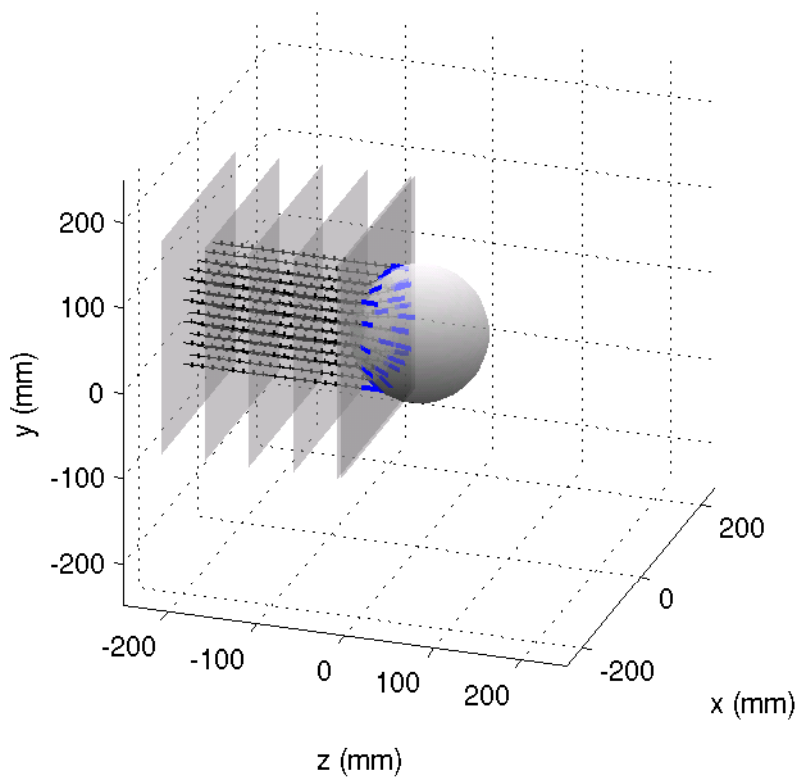**Ray Error (300 m/s Medium, 400 m/s Sphere, 24 kHz)**

Figure 4.13: Ray tracing error for 400 m/s sphere in 300 m/s medium with matched densities for a 24 kHz pulse.

Table 4.1: Concentric Sphere Simulation Variables.

Region	Radius	c	ρ
Inner Sphere (Brain)	65 mm	1500 m/s	1000 kg/m^3
Outer Sphere (Skull)	75 mm	2900 m/s	2000 kg/m^3
Medium (Air)	N/A	343 m/s	1.21 kg/m^3

(a) Side View

(b) Perspective View

Figure 4.14: Ray tracing for 500 m/s sphere in 300 m/s medium and 15 kHz pulse.
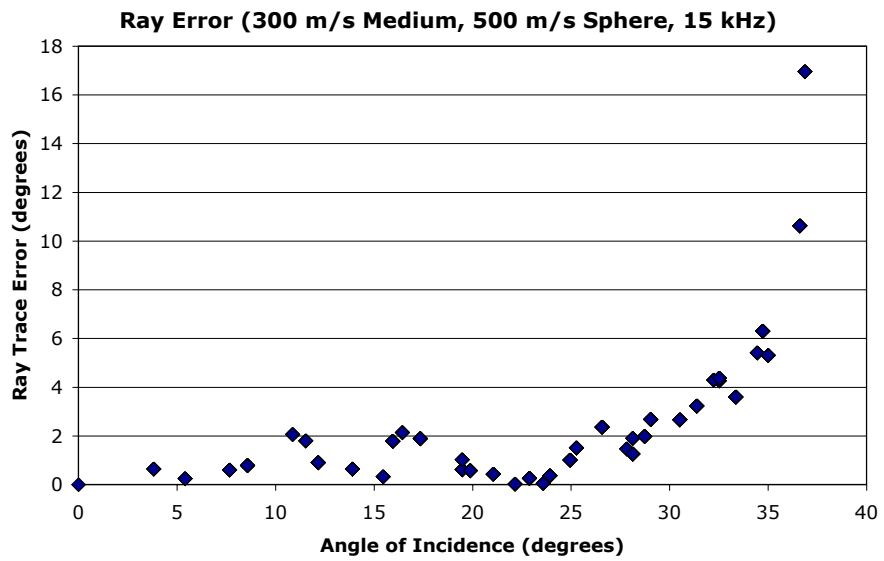
Figure 4.15: Ray tracing error for 500 m/s sphere in 300 m/s medium with matched densities for a 15 kHz pulse.
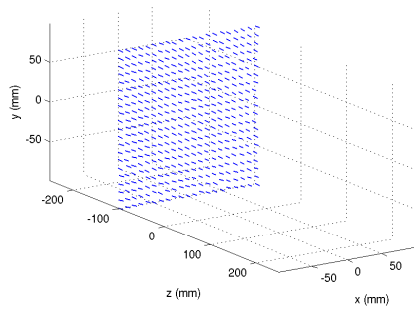
(a) Time: 0.4836 ms
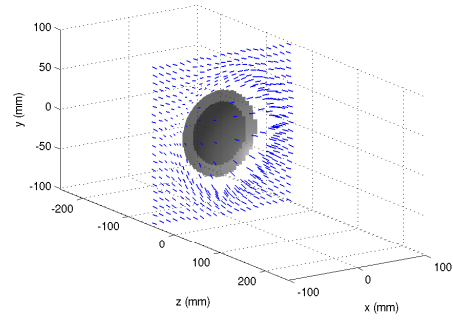
(b) Time: 0.6458 ms
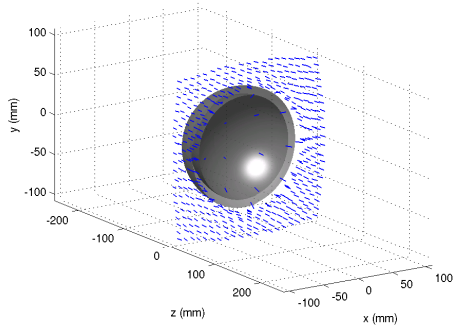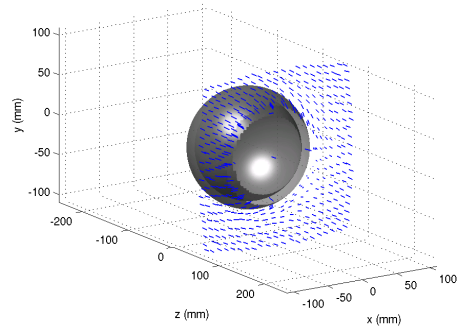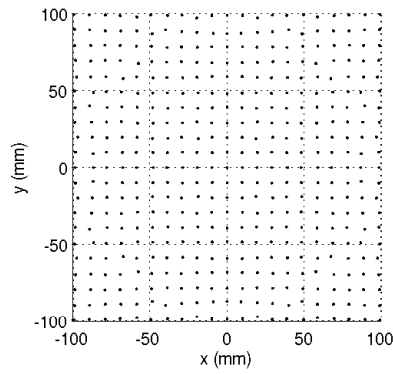
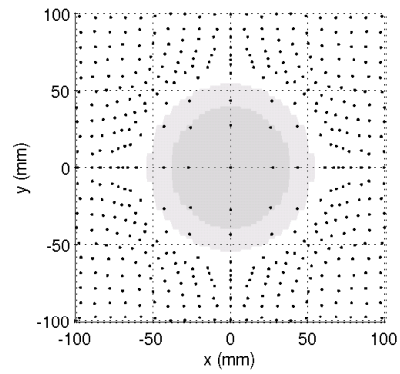(c) Time: 0.8080 ms
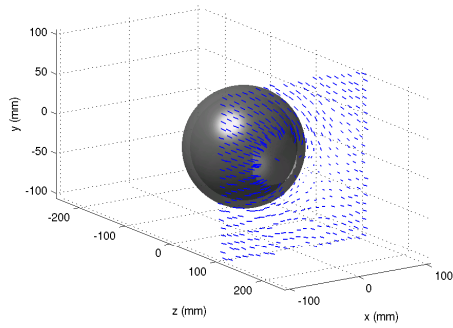
(d) Time: 0.9687 ms
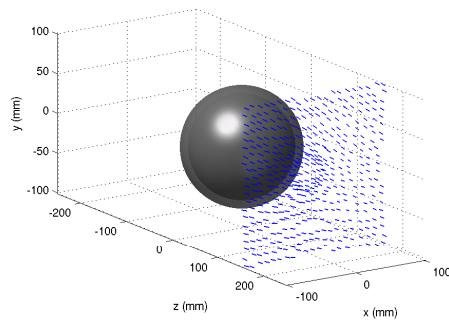
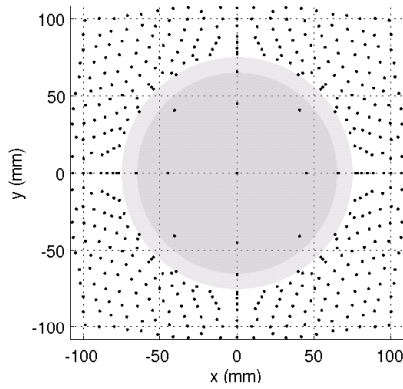(e) Time: 1.1309 ms

(f) Time: 1.2930 ms

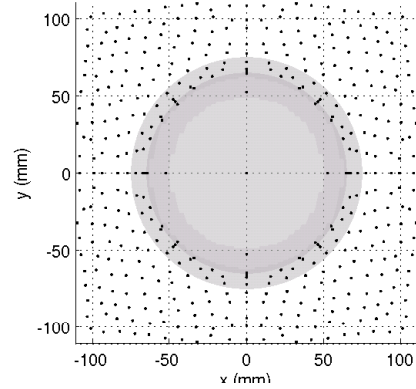Figure 4.16: Ray tracing for concentric fluid sphere simulation.
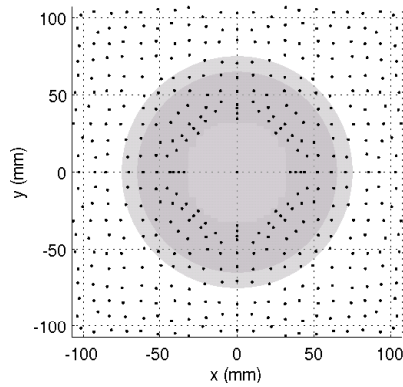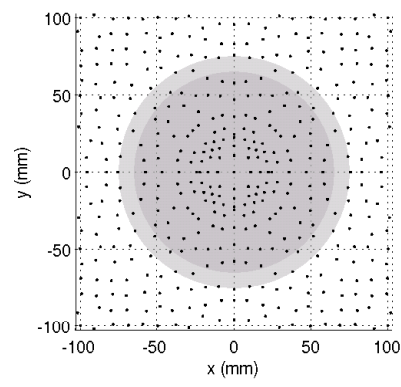
(a) Time: 0.4836 ms

(b) Time: 0.6458 ms

(c) Time: 0.8080 ms

(d) Time: 0.9687 ms

(e) Time: 1.1309 ms

(f) Time: 1.2930 ms

Figure 4.17: Ray concentrations for concentric fluid sphere simulation.

CHAPTER 5

DISCUSSION AND FUTURE WORK

5.1   Discussion

The solution to sound scattering from concentric fluid spheres was first presented. The results were then verified by comparing to the single sphere solution of Anderson [8]. This solution is then later used to obtain data for use in verifying the wavefront reconstruction and ray tracing techniques. This solution is also currently being used to verify a finite element code developed by Dr. Margaret Wismer that will then be used to simulate sound scattering from the human head. Additional applications of this solution include approximating sound scattering from ultrasound contrast agents or cells. The Fourier pulse synthesis method was then derived as a means of performing simulations of finite duration pulses from the time-harmonic solution for scattering from concentric fluid spheres.

Multiple methods were presented to determine wavefronts from pressure data. The first method presented attempted to find the wavefront directly by finding the point that maximized the correlation with a time-shifted reference pulse. This method works well for weak scatterers but fails when the pulse amplitude varies. The remaining methods used an indirect approach to determine the wavefront. The arrival time of the pulse was first determined and then the wavefront was extracted as the set of points with the same arrival time. The first method of this kind used a simple cross correlation between the pulse at a point and a reference pulse. The arrival time was the shift of the reference signal that maximized the cross correlation. This method also works well for weak scatterers but fails when strong reflections occur. The next method used a frequency domain approach to determine arrival times. Since the delay information of a signal is contained in the phase information of a signal, by minimizing the phase, one can determine the arrival time of a

pulse. In theory this should work, but the problem of unwrapping the phase leads to unreliable results. The next method presented determined the arrival time by finding the first peak in the pulse. When noise is not present, this method works well and is fairly accurate. Noise introduces peaks before the onset of the pulse and therefore performs poorly when noise is present. The next method was based on the assumption that the waveform at the position behind the current one is nearly identical to the current one with some time shift. By determining this time shift, one can determine the arrival time between two points. By adding the arrival time differences over the domain, the arrival time can be determined. This method had two main drawbacks. First, the method had a tendency to underestimate the delay when strong reflections occurred. The method was also recursive in nature so the error tended to accumulate as the wavefront progressed. The final method proposed combined the last two methods to achieve the precision of the peak detection method while minimizing the error caused by noise. This was done by first using the peak detection method. If the result was within an acceptable range relative to the last arrival time, the peak detection result was used. If not, the difference in arrival times was computed using the cross correlation of the current signal with the last signal. This method was found to be accurate for most cases and was used for all ray tracing simulations performed later on.

A ray tracing technique for discretized domains was then presented. The idea behind the technique was to break the discretized wavefronts into a series of triangles. From these triangles it is straightforward to compute both the normal of the wavefront and the intersection of a ray with the wavefront. The topic of wavefront was revisited to address the issue of ray quantization. It was shown that the discretization of the wavefronts also discretized the ray directions achievable. This finite set of ray directions impacts the accuracy of the ray tracing computation, so a simple method of reducing the effect of this quantization was presented. The ray tracing technique was then verified by comparing simulation results with Snell's law. The verification showed good agreement with Snell's law. As the error began to increase it was shown that this error was not due to the method but due to the wavelength approaching the size of the sphere.

5.2 Future Work

The ultimate goal of this work is to apply the ray tracing code to FEM simulations of sound wave propagation into the human head. Before that can be done, the ray tracing code still needs to be verified for a wider range of scatterers. The technique was verified in this work for small changes in sound speed (300 m/s to 500 m/s) and no change in density. The human head has a much greater change in sound speed (343 m/s to 3000 m/s) and large changes in density (1 kg/m^3 to 2000 kg/m^3). Accordingly, the code should be verified for this range of values of density and sound speed. The first verification should compare the results of the code with Snell's law as was done here but for a range of sound speeds from 300 m/s to 3000 m/s for matched densities. The single sphere solution could then be used with changes in both sound speed and density in the ranges of interest.

After adequate verification of the ray tracing has been performed, it can then be applied to simulations of the human head. A preliminary model is currently being simulated. This particular model was made from CT scans of the dry human skull shown in Fig. 5.1. A layer of skin was then added by "growing" the skull and then subtracting the original skull. A rendering is shown in Fig. 5.2. The figure also shows a set of ear plugs which was added to the model to see if the occlusion effect is observed with the model. Finally, a brain was added by filling in the volume inside the skull as shown in Fig. 5.3. As can be seen from the renderings, the model is not an accurate representation of a human head. The skin is attached directly to the skull and is missing much of a tissue that would make the model have a more human-like face. The model is also missing the outer ears and nose. A second model is currently being developed using data from a human cadaver. This should be a better representation of a human head since the outer ears, skin, and nose are still intact.
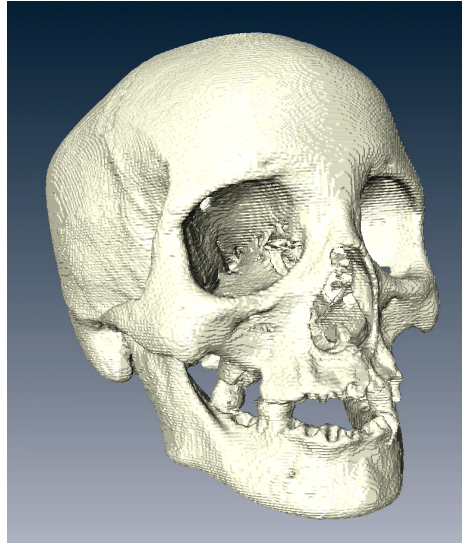
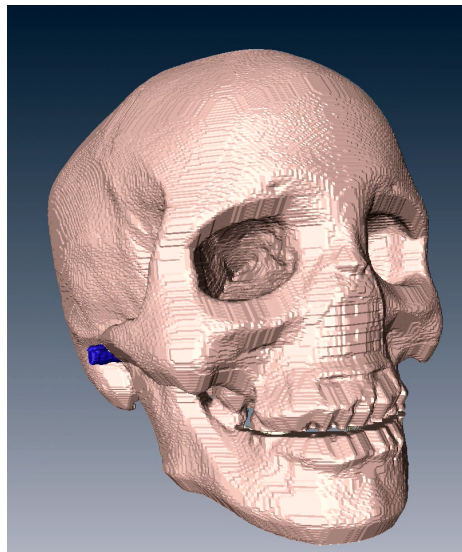Figure 5.1: Rendering of skull used for finite element simulation.

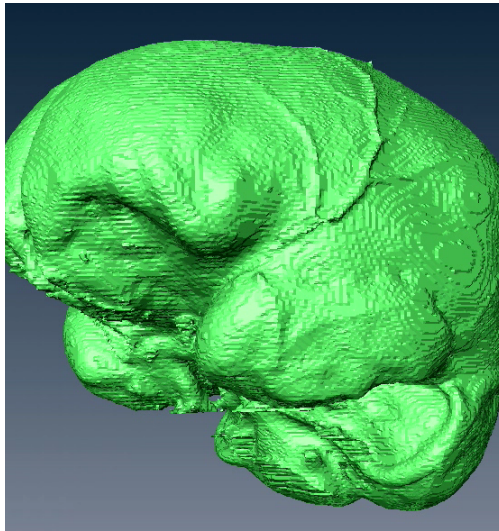Figure 5.2: Rendering of skull used for finite element simulation with skin layer added.

Figure 5.3: Rendering of brain added to model used for finite element simulation.

APPENDIX A

RAY TRACING IMAGES

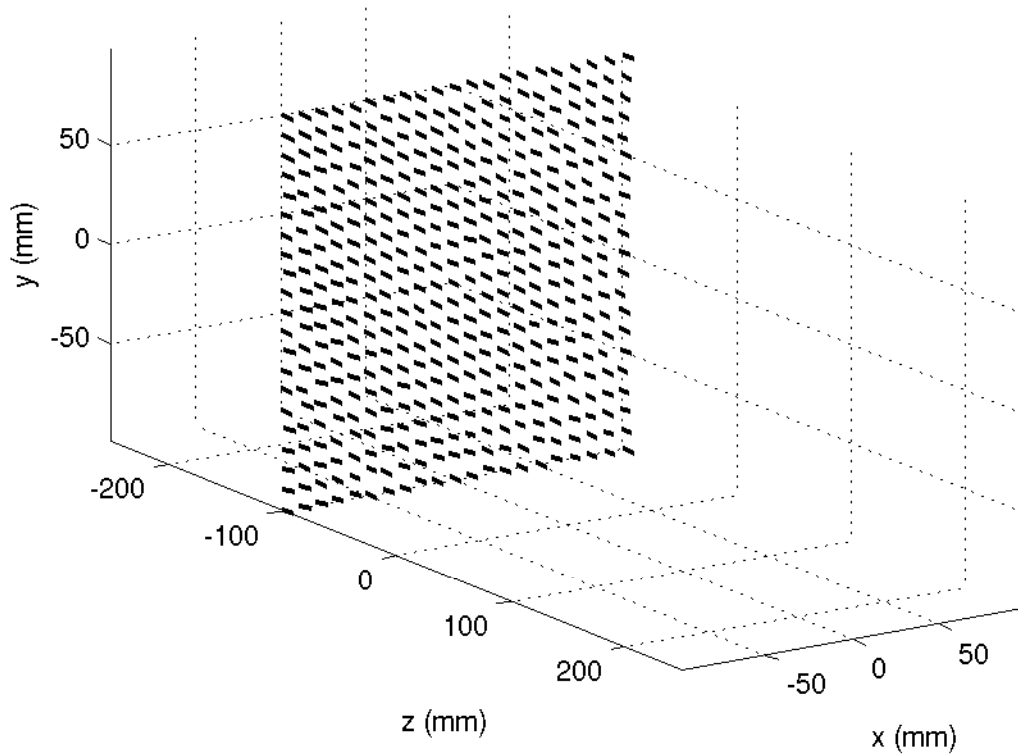To show greater detail, Figs. A.1-A.6 are magnified versions of the images in Fig. 4.16.

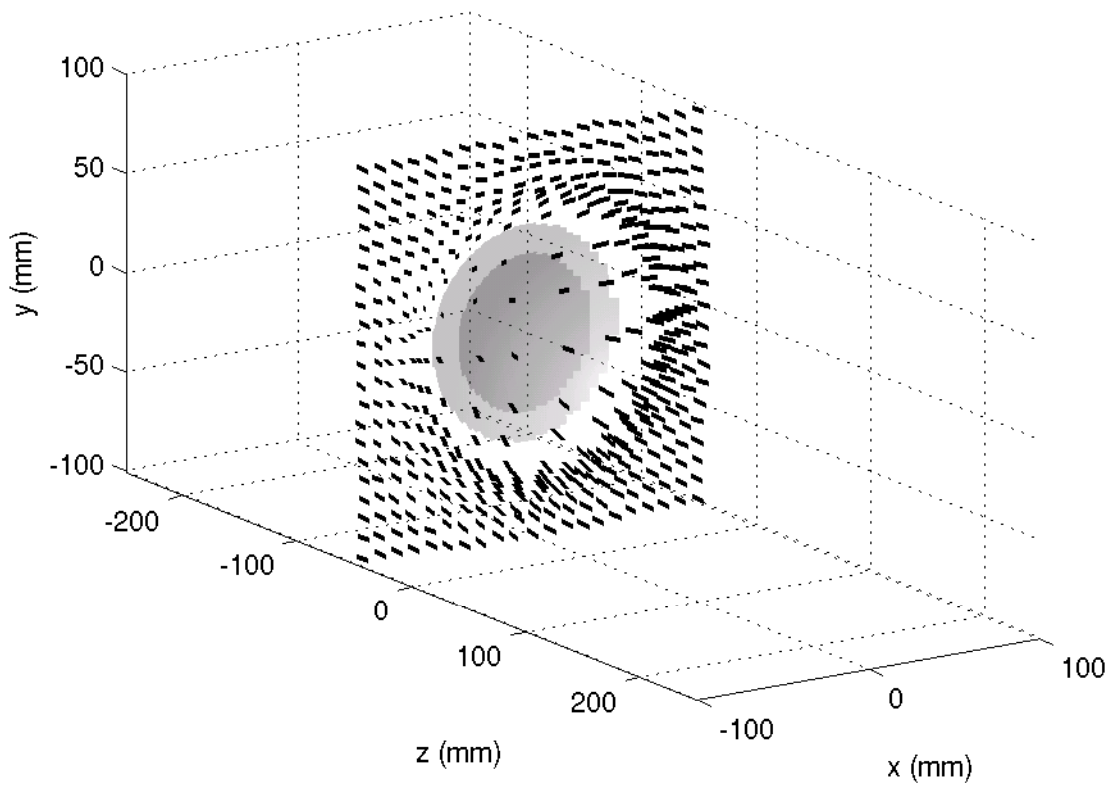Figure A.1: Concentric sphere ray tracing at 0.4836 ms.

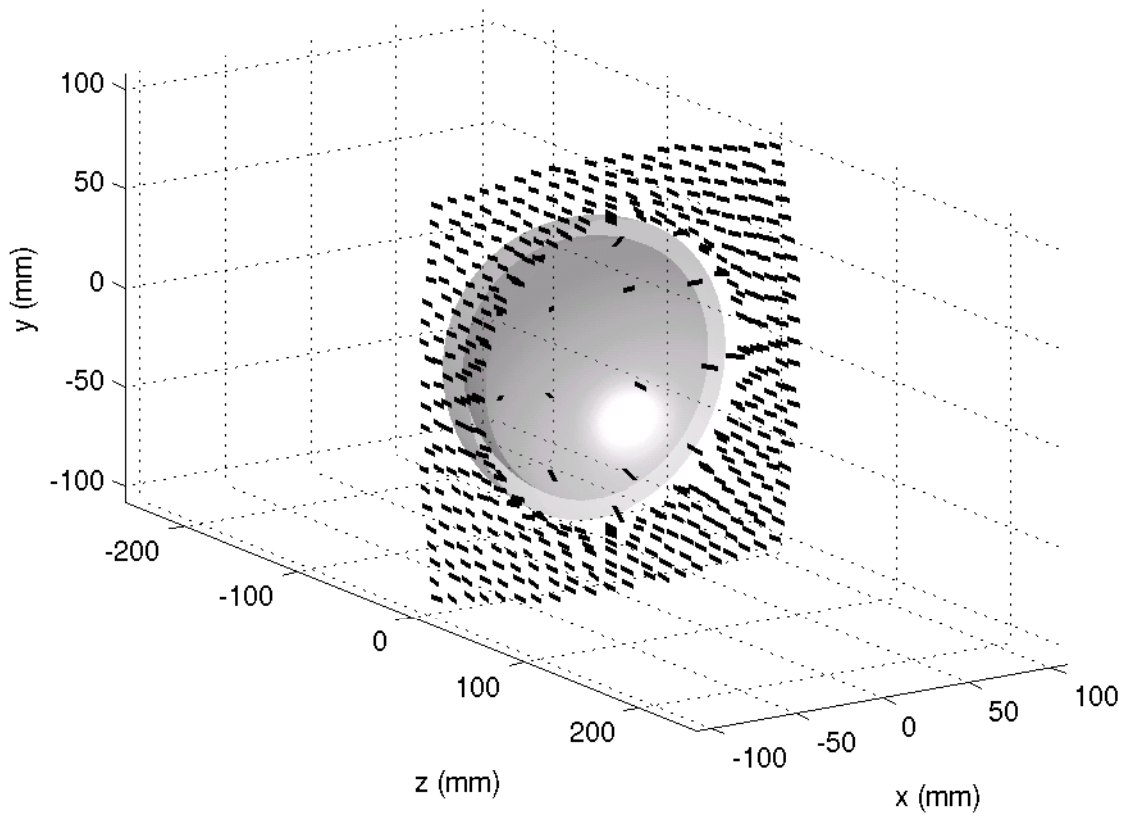Figure A.2: Concentric sphere ray tracing at 0.6458 ms.

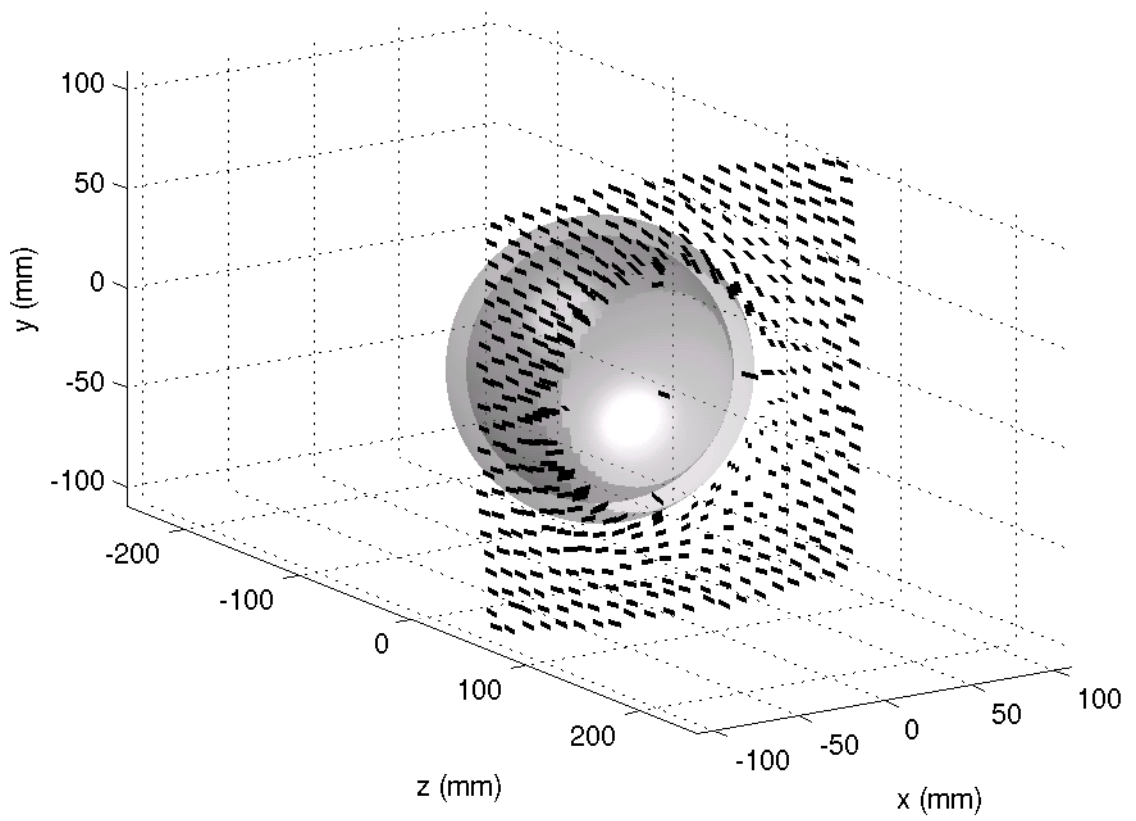Figure A.3: Concentric sphere ray tracing at 0.8080 ms.

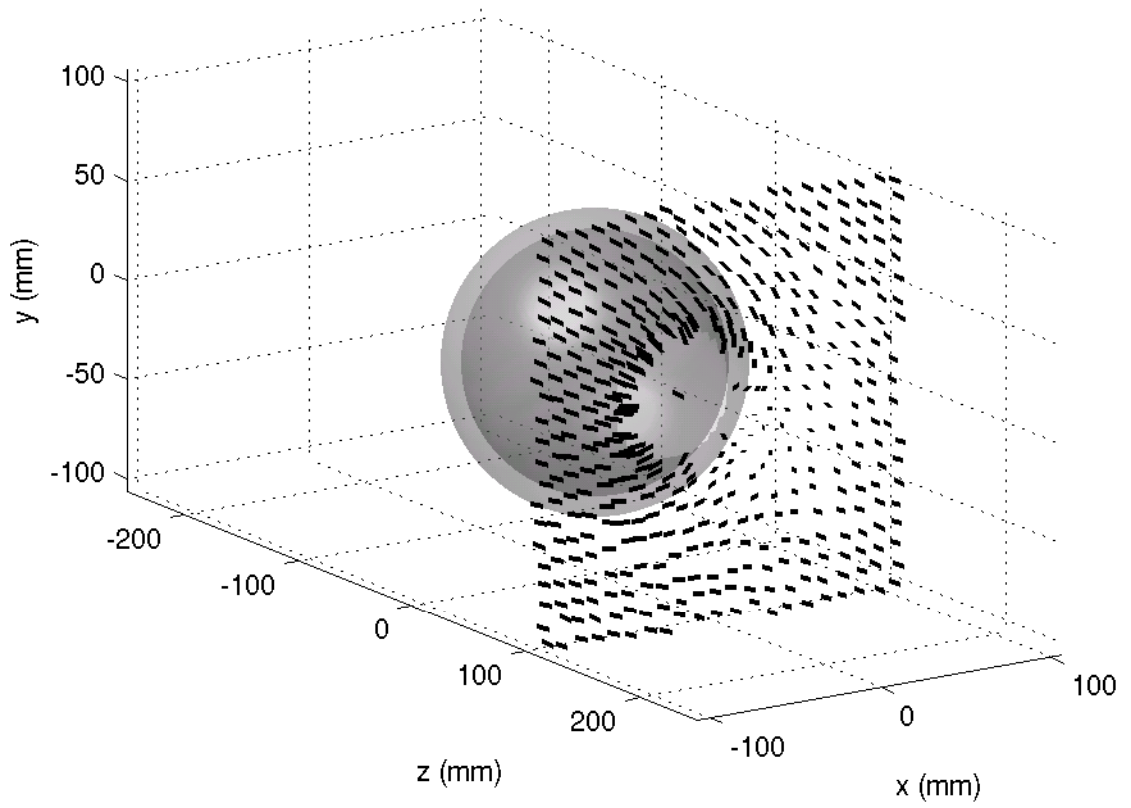Figure A.4: Concentric sphere ray tracing at 0.9687 ms.

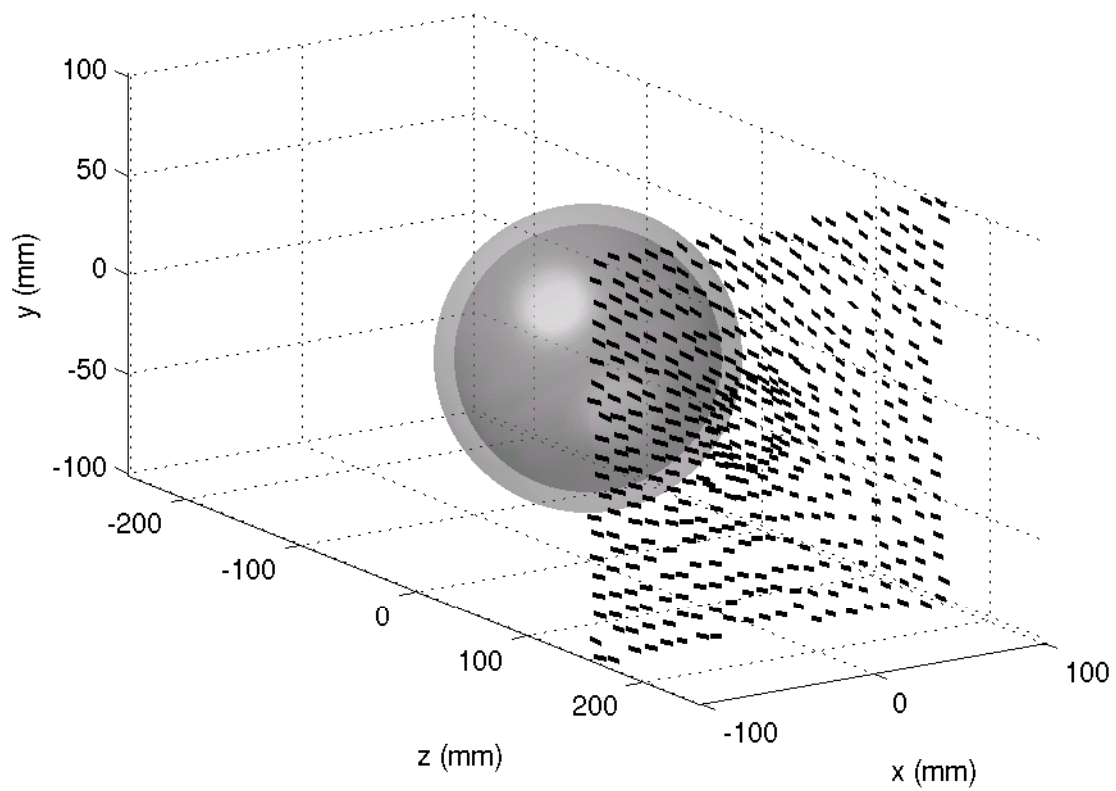Figure A.5: Concentric sphere ray tracing at 1.1309 ms.

Figure A.6: Concentric sphere ray tracing at 1.2930 ms.

REFERENCES

[1] N. I. on Deafness and other Communication Disorders, "Noise-induced hearing loss," September 2002. [Online]. Available: http://www.nidcd.nih.gov/staticresources/health/hearing/NoiseInducedHearingLoss.pdf

[2] E. Berger, "Active noise reduction (ANR) in hearing protection: Does it make sense for industrial applications?" *Spectrum Supplement*, vol. 1, no. 20, pp. 1 – 9, 2002.

[3] E. Berger, "Hearing protector performance: How they work - and - what goes wrong in the real world," *EARLog*, no. 5, pp. 1 – 4, 1996.

[4] G. Rovig, B. Bohnker, and J. Page, "Hearing health risk in a population of aircraft carrier flight deck personnel," *Military Medicine*, vol. 169, no. 6, pp. 429 – 432, 2004.

[5] L. Kinsler, A. Frey, A. Coppens, and J. Sanders, *Fundamentals of Acoustics*. New York, NY: John Wiley & Sons, Inc., 2000.

[6] P. Morse, *Vibration and Sound*. New York, NY: McGraw-Hill Book Co., 1948.

[7] R. Harrington, *Time-Harmonic Electromagnetic Fields*. New York, NY: IEEE Press, 2001.

[8] V. Anderson, "Sound scattering from a fluid sphere," *Journal of the Acoustical Society of America*, vol. 28, no. 4, pp. 426 – 431, 1950.

[9] A. Pierce, *Acoustics An Introduction to Its Physical Principles and Applications*. Woodbury, NY: Acoustical Society of America, 1991.

[10] E. Weinstein. Line-plane intersection. [Online]. Available: http://mathworld.wolfram.com/Line-PlaneIntersection.html